Investigation of hydrogenated V-based systems using ions and photons, a step towards in-situ IBA of metal hydrides

Theofanis Tsakiris

UPPSALA
UNIVERSITET

Dissertation presented at Uppsala University to be publicly examined in Å4101, Ångströmlaboratoriet, Lägerhyddsvägen 1, 752 37, Uppsala, Friday, 20 September 2024 at 09:15 for the degree of Licentiate of Philosophy. The examination will be conducted in English. Chairman of the grading committee: Director of research, Dr. Ian Vickridge (CNRS Délégation Paris B: Paris, Île-de-France, FR).

Abstract

Tsakiris, T. 2024. Investigation of hydrogenated V-based systems using ions and photons, a step towards in-situ IBA of metal hydrides. 62 pp. Uppsala: Uppsala University.

Metal hydrides, based on transition metals, are a promising class of materials for hydrogen storage purposes. Understanding the effects of finite size and the presence of surfaces and interfaces in thermodynamics of hydrogen in these materials is an important step towards engineering hydride-based storage systems. In this work, hydride systems based on vanadium were studied by means of ion beam analysis (IBA), x-ray diffraction (XRD) and optical experiments. A series of thin vanadium films was grown using magnetron sputtering, with the aim of optimizing the growth conditions of the vanadium layer, in order to improve the crystallinity of the produced film. Moreover, the correlation between the optical transmittance and the hydrogen concentration, probed through nuclear reaction analysis (NRA), of a Cr/V superlattice was studied, as a part of an on-going, large-scale investigation of proximity effects. Finally, motivated by the implications caused by the loss of hydrogen during the ex-situ hydrogenation and ion irradiation, a gas-cell aiming at performing IBA with the sample immersed in gaseous environment was designed. The effect of silicon-rich nitride membranes, holding the pressure gradient between vacuum and atmospheric pressure, on the energy and angular distribution of the primary ion beam, was studied theoretically and experimentally, proving the possibility of conducting real-space crystallographic studies using the proposed setup.

Keywords: Metal Hydrides, Vanadium, In-Situ, NRA, IBA

Theofanis Tsakiris, Department of Physics and Astronomy, Materials Physics, 516, Uppsala University, SE-751 20 Uppsala, Sweden.

URN urn:nbn:se:uu:diva-535652 (http://urn.kb.se/resolve?urn=urn:nbn:se:uu:diva-535652)

To my family and friends

List of Papers

This thesis is based on the following papers, which are referred to in the text by their Roman numerals.

I. Tsakiris T., Komander K., Wolff M., Frost R.J.W., Droulias S.A., Pálsson G.K., Primetzhofer D. (2024) Correlation of optical transmittance and hydrogen concentration in Cr/V superlattices. *Nuclear Instruments and Methods in Physics Research Section B: Beam Interactions with Materials and Atoms* 553, 165398. https://doi.org/10.1016/j.nimb.2024.165398.

II. Tsakiris T., Moldarev D., Frost R.J.W., Pálsson G. K., Komander K., Wolff M., Primetzhofer D. (2024). Towards in-situ and in-operando ion beam analysis of metal hydrides in gaseous atmosphere: Conceptual Studies.
In manuscript form.

Contents

Abbreviations

BCC	Body-Centered Cubic
BGO	Bismuth Germanium Oxide (Bismuth germanate)
DC	Direct Current
FWHM	Full Width at Half Maximum
IAEA	International Atomic Energy Agency
IBA	Ion Beam Analysis
IBANDL	Ion Beam Analysis Nuclear Data Library
NRA	Nuclear Reaction Analysis
OSFOLD	Optical Setup FOr gas LoaDing experiments
PIXE	Particle-Induced X-Ray Emission
RBS	Rutherford Backscattering Spectrometry
RF	Radio Frequency
ROI	Region Of Interest
SiRN	Silicon-Rich Nitride
TEM	Transmission Electron Microscopy
TOF-MEIS	Time-of-Flight Medium Energy Ion Scattering
UHV	Ultra-high vacuum
VH	Vanadium Hydride
XRD	X-Ray Diffraction

1. Introduction

1.1. Hydrogen as an energy carrier

In the last 3 decades the global energy demand is continuously increasing [1], with the energy industry still having a strong dependence on fossil fuels and the yearly energy production, through their use, being in the order of 10^{14} kWh [2]. This reliance on fossil fuels has resulted in the release of large quantities of greenhouse gases in the atmosphere, with CO_2 being the main contaminant [3], with the majority of these CO_2 emissions, being the result of covering the energy needs of the industrial, heating and transport sectors [4]. The detrimental environmental impact of the reliance of fossil fuels, along with their limited inventory [5], highlight the need for energy carriers, which can be produced in a sustainable manner.

The utilization of hydrogen, as the primary energy carrier, in the context of a hydrogen economy [6,7], has been considered as a potential solution to the energy crisis, for many years [8]. Both the direct combustion of hydrogen gas [9] or its use in a fuel cell [10,11] can release the stored energy. Fuel cells have been used in the space program for many decades [12] and have begun to also be integrated into road vehicles [13]. Furthermore, both the direct combustion of hydrogen and its use in fuel cells, do not result in CO_2 emissions, thus, a shift towards the use of hydrogen can contribute to the reduction of the annual emission of greenhouse gases. Finally, hydrogen is a non-toxic energy carrier, in comparison to commonly used fuels such as petrol, while it is also characterized by three times higher stored chemical energy per mass, namely 142 MJ/kg [14], compared to hydrocarbons.

Despite being the most abundant element on Earth [15], hydrogen is mainly found in hydrocarbon molecules and water (H_2O), with the molecular hydrogen, namely H_2, corresponding to less than 1 % of the total hydrogen available [16]. The production of additional molecular hydrogen can be achieved through different means [17], with the electrolysis of water [18] being a commonly employed method for “green” production. However, it is important to note that the extent that hydrogen can be considered as a “green” carrier is directly tied to its means of production [19] and their corresponding carbon footprint.

1.2. Hydrogen storage options

The transition towards a hydrogen economy requires reliable means of hydrogen storage. The presently available storage options can be divided into chemical storage, where the energy is stored in chemical bonds [20] and physical storage, which is related to the topic of the present thesis and includes gaseous [21], liquid and solid-state storage options. Concerning the gas storage, the need for high pressures is a major issue, which, in the case of H_2 gas, becomes even more pronounced, due to its low molecular mass. In practice, pressures up to 800 bar are commonly utilized, which correspond to a volumetric density in the order of 40 kg/m^3. The construction and management of high pressure containers, as well as the pressurization process itself are always followed by significant costs [22]. Moreover, further increasing the pressure, to achieve a higher density, is not favored by the physical behavior of the hydrogen gas, which presents non-ideal gas behavior, in these pressure regimes [23]. The flammability of the H_2 gas also introduces major safety concerns, especially in the case of mobile applications. A alternative storage option is the storage of hydrogen in liquid form, which is characterized by a higher achievable density of 70 kg/m^3 [24]. However, the liquification of hydrogen requires low temperatures, with conventional cryogenic tanks operating at 21.2 K [16], which introduces a high energy cost for both the liquification process itself, as well as a high upkeeping cost.

Solid-state storage, which includes the formation of a hydride phase in the material, is an option that has amassed a lot of interest as a potential solution for the hydrogen storage problem, for numerous reasons. First of all, one of the key advantages offered is the elimination of the major security issues, that accompany the conventional storage options. Furthermore, the hydride storage offers the possibility to achieve a higher mass of stored hydrogen per volume, compared to the liquid and gas storage [25]. A description of the properties of the ideal hydrogen storage material, was recently provided by the US department of energy [26]. Specifically, a goal of a metal hydride characterized by 5.5 wt% H gravimetric density is stated, with the long-term goal being 7.5 wt% H. The storage in a temperature range near 100 ^{o}C and close to ambient pressures are also included in the required properties.

There are presently many categories of candidate materials for solid-state storage, but unfortunately none of them meet all the aforementioned criteria. Hydrides based on alkali metals, offer a high gravimetric density, with MgH_2 being the most characteristic example, storing 7.6 wt% H [27]. However, these materials require high temperatures for absorption and desorption [28], at ambient pressures, due to the strong bonds formed. Studies on light materials, such as carbon nano-structures that could potentially achieve high gravimetric densities revealed a need for high temperatures, therefore marking them as an unlikely candidate. The hydride category that this thesis will focus on is the hydrides formed by transition metals.

1.3. Improving the thermodynamic properties of interstitial hydrides

Hydrogen can be absorbed in transition metals and reside in their interstitial sites, in a self-trapped state [29]. An element of particular interest, which will be the main focus of this thesis, is vanadium (V) [30]. It is a light element (Z=23), which is characterized by fast hydrogenation kinematics [31]. These traits mark it as an attractive starting point for engineering a storage material with all the desirable properties. Its bulk properties have been extensively studied [32,33,34,35], but the thermodynamics of hydrogen in vanadium can be further tailored. A common approach to achieve this, is through alloying [36,37]. However, studies over the last decades have also revealed changes in the H thermodynamics that are related to changes in the size of the system [38], the presence of strain [39,40] and even its shape [41]. The reason behind it, is the elastic nature of H-H interactions [42]. The presence of foreign atom species and the resulting proximity effects [43] have also been under investigation in the recent years [44]. Thin films and especially superlattice structures [45] are chosen as samples, due to the tunability of their layers, which allows an in-depth look at all the finite size, strain and proximity effects. Finally, it should be noted that such investigations are relevant even in a bulk hydrogen storage system, since important hydrogen transport phenomena are occurring in the proximity of surface and interface regions.

In order to extract information on properties, such as the electronic structure or the strain in the lattice, in thin-layer metal hydride structures, a wide range of techniques can be employed. The effects of hydrogen intake to the optical properties of materials were noticed early, through induced phase transitions [46], with optical methods, such as “hydrogenography” [47], gradually becoming well-established tools to study hydride systems [48], even within the same phase. Moreover, the volume changes induced in the unit cell from the presence of hydrogen in interstitial positions, are often studied with the means of reciprocal space methods, such as x-ray diffraction (XRD) [49,50]. Studies on resistivity [51] are also a tool to obtain information on the disorder of a hydride system. Finally, gravimetry [52], can be employed in the study of bulk metal hydride systems, but cannot provide information on the physical properties near interfaces. In general, all of these techniques offer limited real-space information on the hydrogen content, because the changes observed in the physical properties under investigation, correspond to the effect of the total hydrogen amount in the sample.

1.4 Aim of the thesis

The ion beam analysis (IBA) methods [53] allow for the extraction of a depth-dependent profile of the distribution of hydrogen, as well as of real-space information on its site location in the crystal, which highlights them as a unique analytical tool for the study of metal hydrides. In this thesis, experimental work on V-based systems, using IBA techniques, is presented. A number of practical analytical challenges, as well as some proposed infrastructure modifications to overcome them are discussed in-depth. Specifically, chapter 2 will include a brief overview of the theory of metal hydride systems, with emphasis on vanadium hydride, while chapter 3 will introduce the key IBA techniques utilized in this work. The study of all the properties discussed in this section, requires a sample of good quality, so chapter 4 will cover the growth and characterization of V films, while commenting on the optimization of some of the growth parameters. Next, chapter 5 involves a study on the optical properties of a Cr/V superlattice structure and their dependence on the hydrogen content. This experiment also highlights some of the practical limitations of studying metal hydrides using IBA methods. A potential solution to such limitations, will be discussed in chapter 6, where a concept for an in-situ setup, aiming towards IBA experiments in a gaseous atmosphere, will be presented in detail.

2. Metal hydrides

2.1. Hydride formation in transition metals

From the perspective of minimizing the energy of a system, the absorption of hydrogen is not equally energetically favorable in all transition metals. An early theory was developed by Nørskov [54], where the energy gain from inserting a hydrogen atom in a volume characterized by a homogeneous density of electrons was calculated. Despite its simplicity, it managed to highlight the general trend of a more energetically favorable hydrogen absorption from the transition metals closer to the left side of the periodic table, which have, in general, lower electronic densities compared to the elements on the right side of the same row of the periodic table.

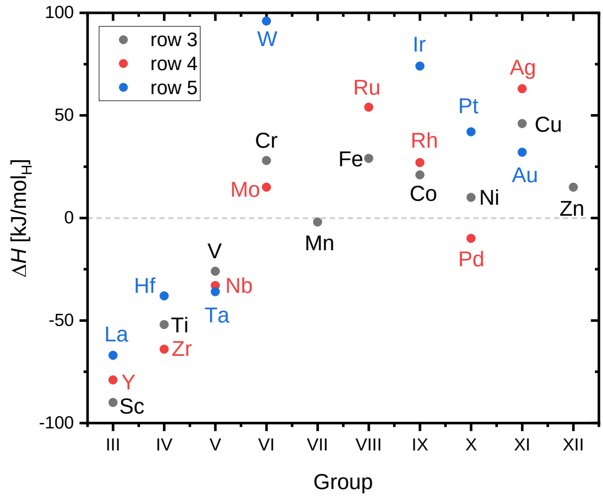

Figure 2.1: Enthalpy of solution for hydrogen absorption, for transition metals in rows 3-5 of the periodic table. Data adapted from [55]

From a thermodynamic point of view, the quantity expressing the energy change per hydrogen atom added to the system is the enthalpy of solution H and it is conventionally expressed in eV per atom or kJ per mole. Figure 2.1 presents experimental data for the heat of solution of different transition metals, for infinite dilution [55]. The elements with a positive heat of solution require energy for the hydrogen intake to occur, in an endothermic reaction, while the elements with negative heats of solution, including V, can absorb hydrogen exothermically. The results in Figure 2.1 experimentally showcase the trend proposed by Nørskov's theory.

2.2. Hydrogen in interstitial sites

In metal hydride systems, where the host lattice is a transition metal (M), the hydrogen atoms will occupy interstitial positions that are characteristic of the lattice structure. For a body centered cubic (BCC) structure, such as V, two types of interstitial sites can be discerned: tetrahedral sites (T) and octahedral sites (O). Figure 2.2 presents a BCC unit cell with two atoms, along with characteristic T and O locations. For the two occupation types, one can extract the maximum number of interstitial sites that are available for hydrogen (H) occupation, namely H/M = 3 for octahedral sites and H/M = 6 for tetrahedral sites. However, those values only represent a theoretical maximum, because, if two H atoms were to occupy neighboring sites they would exhibit a repulsive interaction [56], making such configurations energetically unfavorable. For single element lattices, the highest hydrogen-to-metal ratios observed in most cases are di-hydrides and tri-hydrides.

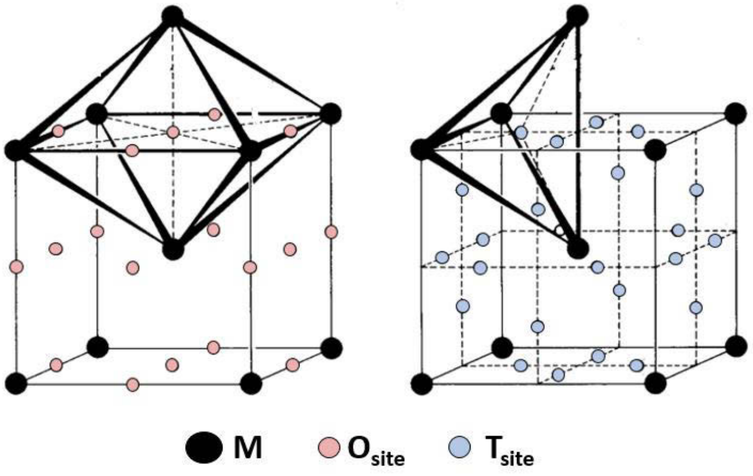

Figure 2.2: Illustration of a unit cell in BCC structure, with the characteristic octahedral (left-side) and tetrahedral (right-side) interstitial site locations being highlighted. Adapted from [57]

2.3. Equilibrium thermodynamics of hydrogen in transition metals

Hydrides are conventionally created by placing a transition metal inside a gaseous hydrogen atmosphere, at fixed temperature and pressure conditions. The thermodynamic potential that is suitable to describe such a configuration is the Gibbs free energy: $G = H - TS$ (2.1). In this equation, *H* denotes the enthalpy, *T* is the absolute temperature and *S* denotes the entropy of the system. In an exothermic reaction, the changes in the Gibbs energy are described by the relation: $\Delta G \leq 0$ (2.2), with *G* being minimized when the system reaches thermal equilibrium. An infinitesimal change in Gibbs energy, in a system at a fixed temperature (*dT=0*) and pressure (*dP=0*), where only one kind of species is added/removed and no work is produced by electromagnetic forces, can be described as:

$$dG = -S * dT + V * dP + \mu dN \xleftrightarrow{dT=0=dP} dG = \mu * dN \ (2.3)$$

The partial differential of the Gibbs energy *G*, with respect to the number of particles *N*, is referred to as chemical potential, which is conventionally denoted as μ and it expresses the energy per atom required to add or remove a species from the system. The chemical potential can be connected to the enthalpy and the entropy changes per atom, at fixed temperature and pressure: $\mu = \frac{dG}{dN} = \frac{dH}{dN} - T * \frac{dS}{dN}$ (2.4). By considering the $MH \leftrightarrow M + \frac{1}{2}H_2$ chemical reaction, the equilibrium between the metal hydride (MH) and the surrounding hydrogen gas requires that: $\mu_{MH} = \frac{1}{2}\ \mu_{H_2}$ (2.5)

In practice, the chemical potential of the hydrogen contained in metal hydride system is not known a priori, but, its value can be obtained from the chemical potential of the H_2 gas, through eq. 2.5. The standard chemical potential, at a fixed absolute temperature T and pressure P_{H_2} can be analytically calculated (Eq. 2.6).In the formula below E_{diss} denotes the dissociation energy of the H_2 molecule, which has an absolute value of 4.477 eV [58] , *K* is the Boltzmann constant and $P_{ref}(T)$ denotes a reference pressure that can be calculated for a temperature of choice and is dependent on the physical properties of the H_2 molecule:

$$\mu_{H_2} = E_{diss} + KT * \ln\left(\frac{P_{H_2}}{P_{ref}(T)}\right) \ (2.6)$$

Metal hydride systems can be described as a lattice gas system [59], which can provide an expression for the chemical potential of the hydride, based on the microscopic properties of the system. In general, this model describes a system of hydrogen atoms, interacting with the host metal atoms and between themselves, denoted as *H-H* interaction. The key assumptions include the H-

H interaction being dependent on the average hydrogen concentration c. Theoretical calculations yield a dependence of the chemical potential on the interaction energy between the hydrogen and the metal host, namely U, and the average *H-H* interaction, namely J: $\mu_{MH} = U + c * J + KT * \ln\left(\frac{1-c}{c}\right)$ (2.7). In the model, the critical temperature for a transition can also be extracted and is dependent on the mean *H-H* interaction energy: $T_c = -\frac{J}{4K}$ (2.8).

2.4. Vanadium hydride

The resemblance of the phase diagrams of metal hydrides based on transition metals, such as vanadium (V), palladium (Pd) and niobium (Nb), to the phase diagrams of one-component systems was initially highlighted by Alefeld [42]. Specifically for the case of V, which is described as "ice-like" in Alefeld's analogy, a detailed phase diagram, for bulk vanadium hydride, referred to as VH, was compiled by Pesch et al. [60]. Figure 2.3 illustrates a part of the VH phase diagram that is relevant to the present work, which is presented in terms of temperature, expressed in ^{o}C, and the hydrogen concentration, expressed in H per V atom. Phase α is characterized by low order in the contained hydrogen. In bulk hydrogen, this phase is characterized by tetrahedral occupation and is referred to as solid-solution phase. The lattice gas model that was presented in the previous section is better suited to be applied in the α phase due to the lack of order, marking it as more suitable for statistical descriptions to be applicable. By increasing the hydrogen concentration, different phases can be formed depending on the temperature. For temperatures below, approximately 200^{o}C, an increase of the H content results in the formation of a new phase, denoted as β. The β phase is ordered, with the hydrogen occupying octahedral positions in every second (110) plane. As the hydrogen concentration is increased, other interstitial positions begin to be filled, resulting in a phase denoted as β'. For higher temperatures the ordered β phases no longer form with the addition of hydrogen, but a high-concentration, disordered α' phase is formed instead.

In both α and β phases, the presence of hydrogen will affect the electronic structure of the host metal. In the case of vanadium, the interstitial hydrogen triggers a hybridization between the 1s orbital of H and 3d band of V, creating new localized electronic states. x-ray emission spectroscopy revealed the most pronounced changes at 7 eV below the Fermi energy [61], while similar results were later obtained by Andersson et al. through first-principles calculations [62]. The metal electrons populating these new states, result in a local weakening of the metallic bonds, leading to a local expansion, which propagates in the lattice. The expansion stops when it is counterbalanced by the repulsive forces exerted to the displaced metal atom, from other metal atoms, further away from the site occupied by H. The H-induced strain field is dependent on the occupancy type, with tetrahedral expansion being characterized by a spherical symmetry, while octahedral is more pronounced on specific directions [40]. These different strain profiles become a practical problem during the transition from α to β phase, when a strain gradient is generated in the material, leading to embrittlement [63].

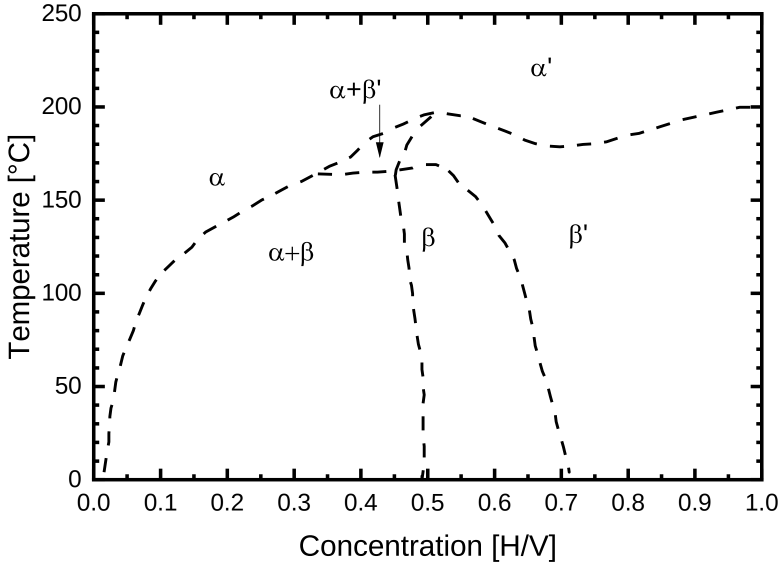

Figure 2.3: Part of the VH phase diagram. Data adapted from [64]

3. Ion Beam Analysis

For several decades [65], ions with kinetic energies in an energy range from few keV/u up to many MeV/u, with *u* denoting the atomic mass unit, have been employed in order to extract information on both the composition and the structure of materials. These so-called *ion beam analysis* (IBA) techniques, allow for absolute quantification of the elements present in a sample, while also featuring isotopic sensitivity, with simultaneous extraction of depth information. In a typical IBA experiment, only an area of few mm^2 of the sample surface is irradiated by the ion beam, with the irradiation resulting in negligible changes to its structure. For this reason, the IBA techniques are considered a virtually non-destructive tool for material analysis. Moreover, IBA techniques are also characterized as "accelerator-based", since large infrastructure is required in order to produce a primary ion beam with kinetic energies above a few hundred keV. The aim of this chapter is to provide an overview on the fundamental physics that govern ion-solid interaction, as well as a selection of the IBA techniques that were relevant to the studies presented in this thesis.

3.1. Ion-Solid Interaction

An energetic ion, of mass M_1, atomic number Z_1 and initial kinetic energy E_0, can interact with both the electrons and the atomic-nuclei of a target material. Each individual collision between two charged particles results in an energy transfer between them. In the case of an ion-electron collision, between the primary beam ion and the electrons of the target, the maximum energy transferred to the electron, namely T_{max}, can be approximated by the formula: $T_{max} \sim \frac{4m_e}{M_1} E_o$ (3.1), which is in the order of $\frac{E_o}{1000}$. The collective result of several such binary collisions is the gradual reduction of the kinetic energy of the primary particle, as it traverses the material, as well as its divergence from a straight trajectory. On the other hand, individual collisions between the ions of the primary beam and the nuclei of the target can result in larger energy transfers between the two and, depending on their masses, in severe deflection of the primary ion from its initial trajectory. Once the primary particle losses all of its kinetic energy, it stops inside the target material. The two separate interaction types, namely electronic and nuclear, between the primary ion and the target are treated separately by theoretical models.

The physical quantity that is conventionally used to quantify the energy losses is the stopping power, denoted as S, which is expressed in units of energy lost per traversed length. It is customary to separate the contributions of the nuclear (S_n) and the electronic (S_e) collisions to the total stopping, due to their different physical origin. The former is the dominant stopping contribution in lower velocities and higher atomic number of primary beams.

For velocities exceeding, approximately, $v=Z_1^{2/3}v_0$, with $v_0 = 2.188*10^6$ m/s being the Bohr velocity, the ion is expected to be stripped of its electrons [66]. In this energy range the electronic stopping is dominant and can be modelled using the formula derived by Bethe: $\frac{dE}{dx_{el}} = \frac{2\pi Z_1^2 e^4}{E} NZ_2 \left(\frac{M_1}{m_e}\right) \ln(\frac{2m_e v^2}{I})$ (3.2). In the previous equation, I denotes the average excitation energy, N refers to the atomic number density of the target, and v is the velocity of the primary particle. For the energy range, corresponding to velocities below $Z_1^{2/3}v_0$, the ion is retaining some of its electrons. In general, the complex topic of the changes in the charge state of an ion and the corresponding stopping power, at low velocity regimes, is still being studied experimentally [67], as well as approached using empirical modelling [68].

The process by which an ion loses energy is purely statistical in nature. Therefore, the amount of kinetic energy lost per unit length traversed in the material will vary for each individual ion of the primary beam. As a result, the kinetic energies of the ions, after they traverse through a slab of a material, will form a distribution. The energy straggling, denoted as Ω, can be related to the full width at half maximum (FWHM) of this energy distribution, which is equal to 2.235Ω. For an ion traversing a path of thickness Δt, in material of atomic density N, the energy straggling can be approximated by the analytical formula calculated by Bohr: $\Omega = 4\pi\, Z_1^2\, e^4 NZ_2 \Delta t$ (3.4). It is noteworthy that in this model the energy straggling is not dependent on the energy of the primary particle.

The existence of analytical models for ion energy-loss and energy straggling, for high velocities, allows for quick calculations in simple systems. However, in order to extract a more accurate estimate on the energy loss of a particle in multi-layered structures with several multi-element layers, the use of a simulation software is considered a better approach. An example of a software package, which is widely adopted by the IBA community, is the SRIM [69] program. This Monte Carlo simulation tool, can aid in the prediction, typically within an uncertainty range of 5-10%, of both the energy and angular distribution of the ions, in a wide range of mass and energy, in multi-layered structures. It is noteworthy that SRIM, still relies on the binary collision approximation and is based on a universal scattering potential [70], with the electronic stopping power being extracted as an integral over the available energy transfers T. Figure 3.1, illustrates the stopping power calculated using the SRIM software, for ^{4}He and ^{15}N ions incident on a V target, over a wide energy range. The two distinct regions of the electronic stopping and their corresponding energy dependence can be clearly seen in both cases, with the ^{4}He stopping power, achieving its maximum at a lower energy, due to its lower atomic number, compared to ^{15}N. Finally, in the case that a more detailed investigation on the stopping power of a specific ion-target pair is required, a collection of experimental data on stopping power is provided by the International Atomic Energy Agency (IAEA) [71].

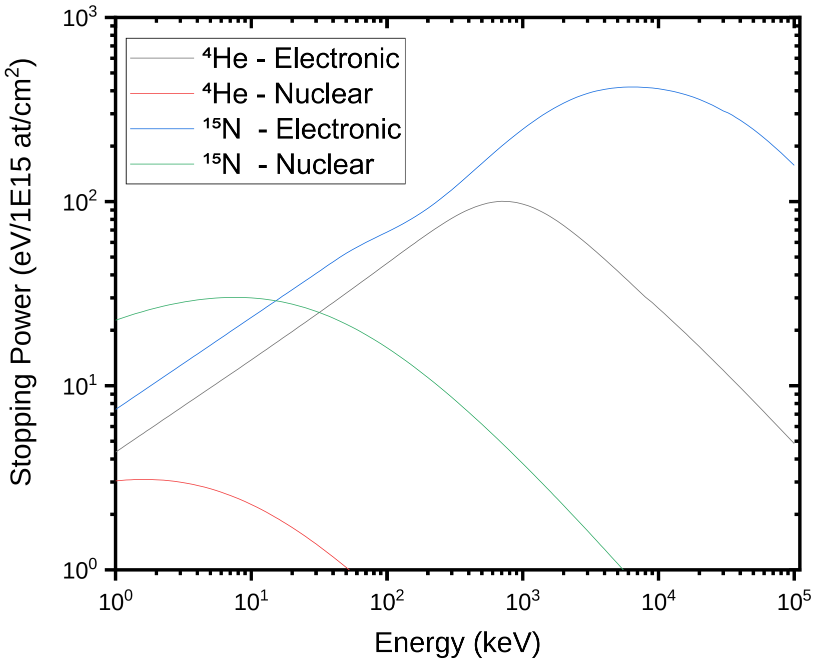

Figure 3.1: The Stopping power of ^{4}He and ^{15}N ions in V, calculated using the SRIM software.

3.2. Kinematics of binary collisions

The interactions of ions with matter are often treated as a sequence of independent two-body collisions. The rest-mass energy of a typical nucleus is in the order of GeV, thus, the motion of ions with kinetic energies up to few MeV can be modeled using non-relativistic formulas. For primary-beam ions of mass M_1, illustrated as green circles in Figure 3.2, with a kinetic energy equal to E_0, being elastically scattered towards an angle θ from a target nucleus of mass M_2, illustrated as red circles, the conservation of energy and momentum principles can be used to extract the kinetic energy $E_1=K_b E_0$ of the projectile after the collision. The quantity K_b is referred to as kinematic factor and is independent of the energy of the primary beam and the interaction mechanism, namely electrostatic or nuclear and can be calculated by Eq. 3.5. In the case that $M_1<M_2$, the kinematic factor increases with increasing M_2, since scattering from a heavier target results in more energy retained by the projectile.

$$K_b = \left[\frac{\left(\sqrt{1-\frac{M_1}{M_2}\sin(\theta)}+\frac{M_1}{M_2}\cos(\theta)\right)}{1+\frac{M_1}{M_2}}\right]^2 \quad (3.5)$$

In the case that $M_1>M_2$, i.e. a heavy projectile being scattered by a lighter target, the projectile cannot be backscattered and it is confined within a scattering cone with a half-angle equal to a maximum deflection angle θ_{max}, which can be calculated using the formula: $\cos^2(\theta_{max}) = 1-\left(\frac{M_2}{M_1}\right)^2$ (3.6)

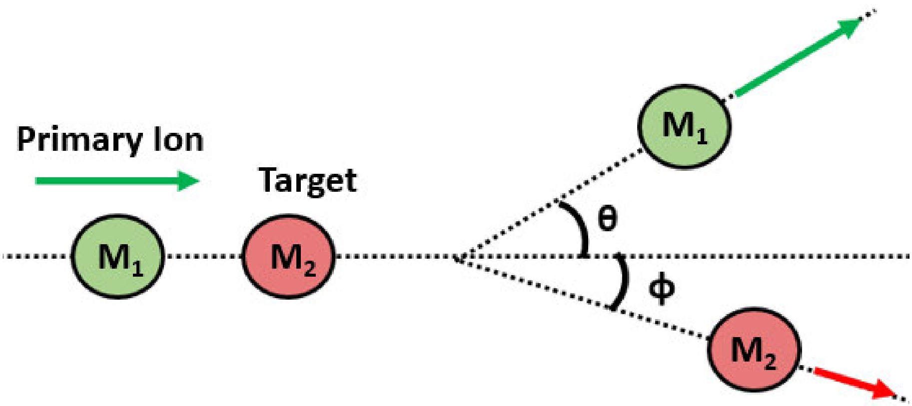

Figure 3.2: Simplified illustration of a binary collision between primary ion (green) and target particle (red).

The kinematic expressions for the elastic scattering are valid regardless of the type of forces exerted between the ion and the target, i.e. electrostatic or nuclear, but do not contain any information on the probability of the elastic interaction to occur. The physical quantity expressing the probability of a primary particle, with a fixed kinetic energy, to be scattered from an impact parameter element $d\sigma$ into an infinitesimal solid angle $d\Omega$, at an angle θ, is the differential cross-section: $\frac{d\sigma}{d\Omega}(\theta)$. The nature of the interaction between charged ions and nuclei is dependent on the kinetic energy of the ion and the electrostatic Coulomb barrier between them. If the kinetic energy of the primary ion is not sufficient to exceed the Coulomb barrier, the interaction is then purely electrostatic and the scattering cross-section is expressed by the Rutherford differential cross section formula [72]. An expression for Rutherford's formula, is given by the analytical equation: $\frac{d\sigma}{d\Omega} = \frac{\left(Z_1 Z_2 e^2\right)^2}{(4E)^2} \frac{1}{\sin^4(\theta_c/2)}$ (3.7), which is valid in the center-of-mass frame. For the case of high-Z target nuclei, a correction is needed due to the screening of the nuclear charge from the 1S orbital electrons. For backscattering angles above 90°, the analytical formula by L'Eculier [73] can provide a satisfactory correction.

If the kinetic energy of the particle is high enough to overcome the Coulomb barrier, or sufficient for the particle to have a non-negligible probability to bypass the barrier through quantum-tunneling, then Rutherford's formula no longer applies. In order for the IBA techniques to remain applicable in this energy regime, experimental data must be available for the cross section of the interaction between the primary beam and the light elements present in the target. A collection of experimental cross-section data is publicly accessible in the IBANDL online library [74]. Finally, some sets of experimental data have been further evaluated, using complementary theoretical calculations [75], in order to allow interpolation for angles and energies that have not been directly measured experimentally. Such datasets are referred to as "evaluated datasets" and can be generated via the SigmaCalc tool [76].

3.3. Rutherford Backscattering Spectrometry (RBS)

The analytically-known kinematics of both the binary collisions and the electronic stopping power at high velocities, allow charged ions to be used as a tool to extract structural information. In order to detect heavier elements in a matrix comprised of lighter elements, a light primary beam and a backscattering geometry is conventionally chosen. The energy of the beam is also tuned to a regime where the interactions with the target's nuclei are of electrostatic nature and therefore the cross-section of the interaction is analytically known. This method is referred to as Rutherford Backscattering Spectroscopy (RBS), with 2 MeV ^{4}He ions, being a commonly employed primary beam to study most elements that are heavier than carbon. The energy of a particle backscattered from a nucleus at depth *t*, for an incidence angle α of the primary beam and an exit angle β of the scattered beam particle can be analytically calculated using equation 3.8:

$$E_{detected} = K_s(\theta)\left(E_0 - \int_0^{t/\cos(a)} S(E)dx\right) - \int_0^{t/\cos(b)} S(E)dx \quad (3.8)$$

In the context of analyzing thin films, such as metal hydride layers, that are deposited on light substrates, the RBS technique can provide accurate information on the thickness of the layers, expressed in units of atoms/cm^2, as well as information on the layering order and roughness.

Finally, in order to facilitate the data analysis procedure, software packages are often utilized, as they integrate all the analytical equations needed for the analysis, along with empirical and experimental data on the stopping and cross-sections. For the analysis of RBS data, SIMNRA [77] is an example of a commonly used software.

3.4. Ion Channeling & Blocking Patterns

Initially discovered in computer simulations [78], the channeling effect originates from the structure of the target material. Numerous, naturally occurring materials, as well as artificially created nano-structures, present a high degree of crystallinity, therefore, the channeling effect is of high importance in the interpretation of experimental data. When a charged particle travels through a crystalline material in a direction that is aligned with a major crystalline axis, it undergoes a series of small-angle collisions and is steered away from the scattering centers. The result is a change in the number of the scattered particles for this orientation of the sample.

The presence of crystallinity can also affect backscattered particles. If the exiting direction of a particle, after the scattering, is aligned with a crystal axis, then a shadowing effect occurs, with the particles being blocked from exiting in that particular direction. The blocking patterns and the channeling patterns are extremely similar, for a fixed energy of primary beam [79] and, in theory, with the correct sample orientation and detector placement it is even possible for the two effects to occur simultaneously. Since the effects originate from the crystalline structure, they can be utilized in order to extract crystallographic information on an unknown structure. Additionally they can allow for the study of structures that are distorted by stress [80]. Examples in vanadium structures, relevant for the metal hydride research, will be presented in the following chapters.

3.5. Particle-Induced X-Ray Emission (PIXE)

A technique that is often employed simultaneously to the RBS, is called Particle Induced X-ray Emission (PIXE) [81]. The interaction of the primary ions with the electrons of target material creates vacancies in the electronic levels, due to the kinetic energy transfer that occurs. Electrons from higher energy levels can then undergo a transition to fill the existing vacancy. The energy difference, which is characteristic for each element [82], can be either be emitted in the form of a photon, i.e. the characteristic x-ray, or be transferred to an Auger electron. The decay rates of the atomic levels can be calculated theoretically [83], but, overall, the x-ray emission probability decreases with decreasing atomic number of the target atom. The PIXE technique can be utilized for qualitative analysis of the elemental content of a sample, but the extraction of quantitative information can be quite complex and is outside the scope of the present thesis.

3.6. Nuclear Reaction Analysis (NRA) for hydrogen detection

In order to study the depth profile of hydrogen in a material of interest, which in this case is a metal hydride system, the nuclear reaction analysis (NRA) technique is conventionally employed. For the detection of hydrogen, the nuclear reaction $^{1}H(^{15}N,\alpha\gamma)^{12}C$ has been of particular interest for many decades [84], due to a narrow 1.8 keV resonance occurring when the energy of the primary particle is equal to E_R = 6.385 keV, measured in the frame of reference of the laboratory [85]. After the nuclear reaction takes place, a ^{12}C nucleus is created in its first excited state [86], which afterwards relaxes to the ground state, with a simultaneous release of a characteristic 4.4389 MeV gamma-ray. The resonance cross section is approximately 20000 times higher than the corresponding off-resonance cross section, reducing the contribution of the latter to a negligible fraction of the produced gamma-ray yield and therefore ensuring that the detected yield is proportional only to the hydrogen content of a specific depth inside the sample.

A typical NRA experiment, aiming at detecting H, involves irradiating the sample with ^{15}N ions of different kinetic energies, starting from an energy slightly lower than the resonance energy and increasing the energy in steps. As a ^{15}N ion, with initial energy $E>E_R$, traverses the material, its kinetic energy gradually drops, eventually reaching the resonance energy and yielding a high gamma-ray yield. Afterwards, the particle will continue losing energy until it comes to rest, producing a negligible off-resonance gamma-ray yield. A depth scale can be extracted from the energies used, only if the stopping power of the ^{15}N ions is well known. Finally, the depth resolution of the technique is dependent on the stopping power of the ^{15}N ions on the target material and the energy resolution available. Specifically for V, the stopping of ^{15}N ions has been recently evaluated [87]. Despite the width of the resonance being less than 2 keV, the presence of a doppler effect, originating from the zero-point vibration [88] of the confined hydrogen results in a deteriorated energy resolution, in the order of 12 keV, near the surface. For most materials the resulting depth resolution, for hydrogen detection using ^{15}N, is in the order of few nm.

4. Growth and Characterization of thin V films

During the duration of the dissertation, more than fifty thin V epitaxial samples, with V layer thicknesses in the range of 20-80 nm, were synthesized and characterized. The growth process took place in the sputtering setup that is located at the Tandem Laboratory, at Uppsala University. The initial sample batches were grown for the purpose of optimizing some of the V growth parameters, while the samples that followed had their layers tailored to facilitate different types of studies, including medium energy ion scattering (MEIS) cartography. In this chapter an example of a 2D MEIS crystallographic map obtained from a thin V film is presented. In general, the V films were prepared for a wide range of studies including MEIS cartography of H-loaded V layers, studies on H desorption and ion-assisted H loading, but the details of those studies are not part of the present thesis.

4.1. Sample growth

The V thin films were grown through DC and RF magnetron sputtering [89], on single-crystalline MgO (001) substrates. Before the growth, the background pressure in the chamber was of the order of 10^{-8} mbar. This ultra-high vacuum (UHV) environment was vital to reduce the presence of contaminants in the grown film. The substrates were kept at a temperature range of 280-320 ^{o}C, measured through a K-type thermocouple. In practice, the current of the resistive heater was being set to a desired value in the range of 2.8-3.2 A. The substrate temperature, during the growth, was in the range of 280-320^{o}C and it was continuously monitored over time, in order to ensure that thermal equilibrium had been achieved, which corresponded to a temperature stability within 0.1 ^{o}C. The sputtering of the V layer took place in argon (Ar) atmosphere, with the Ar gas being supplied to the vacuum chamber through a mass-flow-control system. The stability of the Ar plasma, was dependent on the flow values set, ranging within 5.3-5.7 sccm, with a throttle valve, which was controlling the access to the turbomolecular pump sustaining the vacuum, being set to 78% opening. The pressure readings, during the sputtering process, were obtained through a gas-dependent cold cathode gauge (Pfeiffer IKR 361). A pressure-dependent correction factor, provided by the manufacturer, was applied to extract the pressure range, namely $5 - 12 * 10^{-3}$ mbar. The substrates were fixed on a rotating stage, with a rotation rate of 10^o/sec, in order to ensure lateral homogeneity. During a single growth cycle, the growth conditions were reproducible. Before the sputtering process, the growth rate of the different layers was estimated using a quartz crystal microbalance [90], in order to choose the growth time needed to reach the desired thickness.

Bulk crystalline V crystal is characterized by a body-centered cubic structure, with a lattice constant equal to 3.024 Å [91], while MgO is characterized by a halite structure, with a lattice constant of 4.214 Å [92]. The registry of a V layer to an MgO substrate is thus possible only if the former is grown rotated by 45^o in-plane. In other words, the <100> crystalline direction of the V is parallel to the <110> direction of the MgO. Moreover, the atomic distance in the <110> direction of MgO is 2.98 Å, which is lower than the lattice constant of V, resulting in a compressive, in-plane stress being applied to the V crystal. An elastic response is then triggered, leading to an out-of-plane expansion. The strained V layer therefore exhibits a body-centered tetragonal symmetry. The out-of-plane expansion has been quantified, in past studies, to be in the order of 1.5% [93].

Next, a thin palladium (Pd) layer was grown, for oxidization protection purposes, while the samples were still at high temperature. The pressure of the Ar gas, during the Pd growth was equal to $1.5 * 10^{-2}$ mbar. The thickness of the Pd layer varied in the 1-7 nm range, depending on the type of the experiment the sample was being produced for. For example, in the case of a sample tailored for blocking pattern mapping, the thickness of the Pd layer was reduced to minimize the de-channeling effect on the outgoing particles. The Pd layer is not expected to be epitaxially grown due to a significant lattice mismatch with the V underlayer. The Pd layer also allows for the spontaneous dissociation of H_2 molecules, leading to accelerated thermal hydrogen loading capabilities. Finally, a thin aluminum oxide (Al_2O_3) capping was deposited, after the sample had cooled down to room temperature. The pressure of the Ar during the Al_2O_3 growth was the same as during the Pd growth. The oxide coating sets a potential barrier [94], which allows the retention of any hydrogen introduced in the V layers, during an ion irradiation, as well as during a thermal hydrogen loading process. In each batch, an amorphous C substrate was placed next to the MgO substrates. The sputtering deposition would then result in the production of polycrystalline V layers, on top of the C. These samples were produced to quantify, through RBS measurements, the amount of O in the V layers, which never exceeded few %.

4.2. Study of sample structure through IBA

The structure of all grown samples was characterized using IBA methods. Figure 4.1 presents a typical RBS spectrum, obtained from an Al_2O_3/Pd/V/MgO structure, using a primary beam of 2 MeV ^4He. The backscattered particles were detected using a solid-state detector, fixed at a detection angle of 170°, with an energy resolution, for ^4He particles, in the order of 14 keV. Since the samples were epitaxial structures, the <001> channel of both V and MgO layers is parallel to the surface normal. In order to avoid any channeling effects, the sample was tilted by 5° and its orientation was simultaneously varied within an additional two-degree range during the acquisition of the RBS spectrum. The backscattering signal from Mg atoms was used to normalize the solid angle-charge product, since the ^4He-Mg interaction is electrostatic, in this energy range, and thus the cross section is analytically known. For the RBS spectrum, the conversion factor from channels to energy was obtained by scanning bulk reference samples of high purity, since the ions backscattered from their surface reach the detector with a known energy, that is equal to: $K_b(M_2) * E_0$.

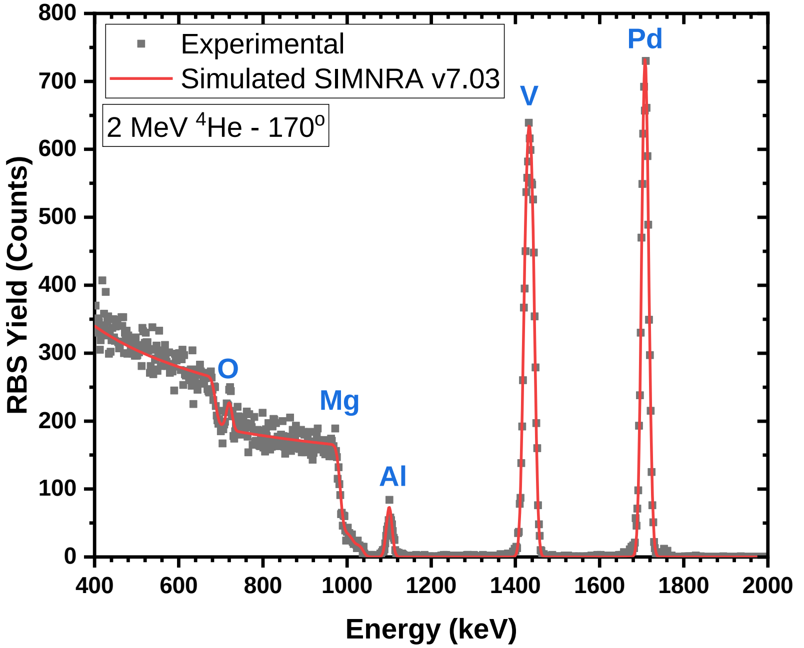

Figure 4.1: Typical RBS spectrum for an Al_2O_3/Pd/V/MgO structure. The elastic scattering peaks are labeled. The red curve represents a fit using SIMNRA 7.03 software.

In the sample corresponding to Figure 4.1, both the V and the Pd layers are too thin, compared to the depth resolution of the measurement, so their RBS signal appears as a gaussian-shaped function. Figure 4.1, also illustrates a fit calculated through SIMNRA software. In the presented fit, the layer thicknesses obtained for Al_2O_3, Pd and V layers are 117, 44 and 204 * 10^{15} at/cm^2, respectively. Using the density of bulk V, an approximate thickness value of 29 nm can be extracted, which, at a first order, is close to the nominal one, namely 25 nm. It should also be noted that the density of V changes when it is in a strained state.

A complementary PIXE spectrum, was simultaneously acquired, in order to ensure the absence of contaminants in the samples. The PIXE data was not used for any quantitative analysis, but for a qualitative study of the elements present in the sample. Figure 4.2 illustrates a typical PIXE spectrum, from the same sample, with two peaks from V-K_α and V-K_β lines being the most pronounced. A mixed signal comprised of the L_α and L_β lines from Pd and the Ar-K_α line was observed in the energy range near 3 keV. Finally, the lower energy range, shows less pronounced peaks corresponding to the K lines of magnesium (Mg) and aluminum (Al).

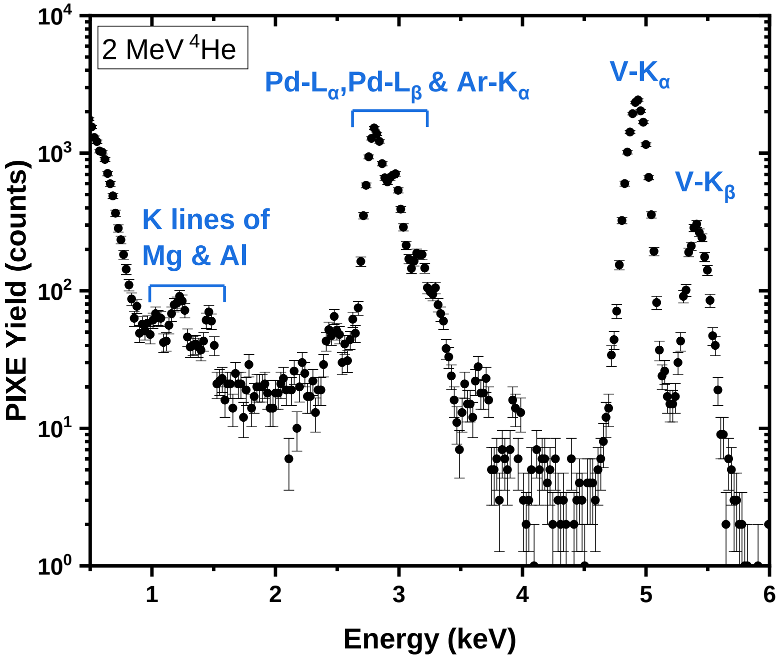

Figure 4.2: Typical PIXE spectrum for an Al_2O_3/Pd/V/MgO structure. The characteristic x-ray peaks are labeled.

4.3. Study of sample crystallinity

The crystallinity of the samples was evaluated, through θ/2θ x-ray diffraction (XRD) scans. The primary x-rays used were Cu-K_α, with the weighted characteristic wavelength of $K_{\alpha 1}$ and $K_{\alpha 2}$ being equal to 1.5418 Å, with the x-ray source and the detector maintaining a Bragg-Brentano geometry, during the scan. In this configuration, the momentum transfer vector $\boldsymbol{Q}$ is parallel to the surface normal of the epitaxial structure. Figure 4.3 illustrates a typical XRD spectrum, for the same V sample. The peaks of the (002) and (004) reflections of the MgO substrate are the most pronounced, with the V (002) peak being visible at 2θ angle of 60.7°. Using Bragg's law [95] and assuming an error of $\delta\theta=0.02^o$ in the setup, a value of 3.056±0.001 Å was obtained for the out-of-plane lattice parameter, verifying the presence of initial strain. Using the extracted FWHM values and Scherrer's formula [96], a coherence length could be extracted, which was, for most samples, in the range of 22-27 nm.

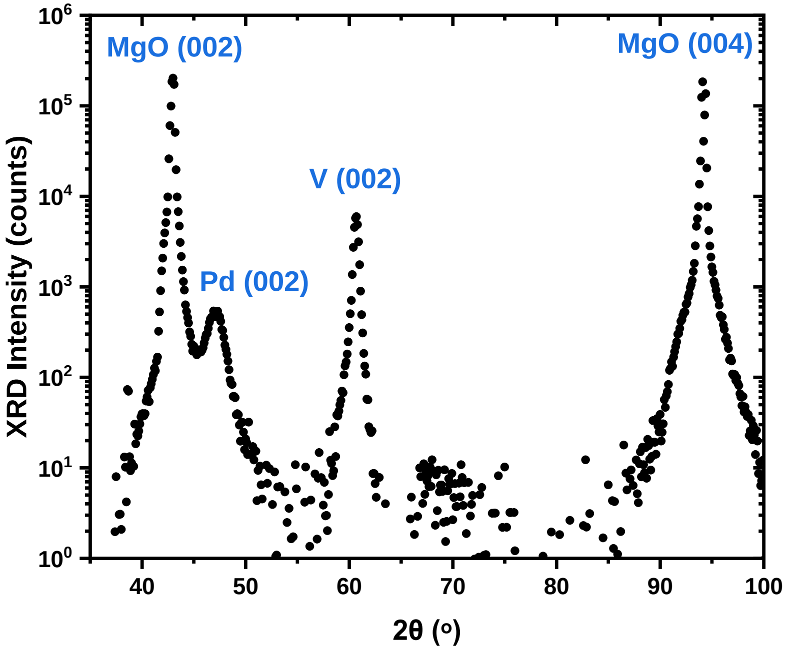

Figure 4.3: Typical XRD spectrum for an Al_2O_3/Pd/V/MgO epitaxial structure.

The FWHM of the V (002) peak was chosen as the main comparison factor, to estimate which samples were of better crystal quality. No rocking curves were recorded for the samples. Figure 4.4 illustrates some of the FWHM values obtained in the early stages of the project, for different combinations of pressure readings and heater currents. The lowest pressure values were accompanied by plasma instabilities, which resulted in deteriorated crystal quality. The FWHM values, for fully-coherent V superlattices, of similar thickness to our samples, that are available in the literature [93], are also included in Figure 4.4, in order to indicate a lower limit for the FWHM value. In practice, the thin V films are expected to exhibit an elastic relaxation as they grow further away from the MgO/V interface, which will result in higher FWHM values, compared to a Fe(Cr)/V superlattice, which is characterized by a homogeneous strain profile, due to its intermediate layers. The FWHM obtained using a 3.2 A current in the heating unit, which corresponded to a temperature of 298±2 ºC, and an effective Ar pressure of $7 * 10^{-3}$ mbar, approximately, was deemed as satisfactory at that stage and set as a reference point for all the future growths.

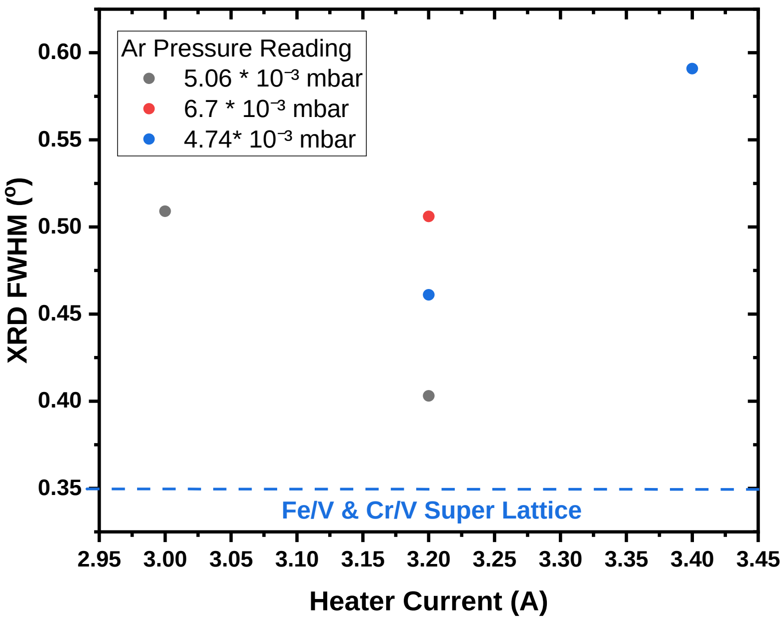

Figure 4.4: FWHM of the V (002) reflection peak in XRD, for different growth parameters of thin V films. The horizontal dotted line expressed the corresponding FWHM of V superlattices of similar thickness.

Finally, a complementary real-space view on the crystallinity of the samples was obtained through the study of blocking patterns, in the ToF-MEIS setup at Uppsala University. The setup is equipped with a position-sensitive detector, with a radius of approximately 6 cm, which is fixed at a distance of 29 cm from the sample, thus covering an angular range of 22º. Figure 4.5 illustrates the blocking pattern of the <001> channel, obtained using a sample that covered with a Pd layer of sub-nm thickness. The sample was irradiated with a pulsed beam 200 keV H_2^+ ions, while rotated by 20º, to ensure irradiation in the random direction, and the center of detector was approximately aligned with the <001> channel, to record the blocking pattern of the backscattered particles. In Figure 4.5 both axial and planar channeling patterns are clearly visible.

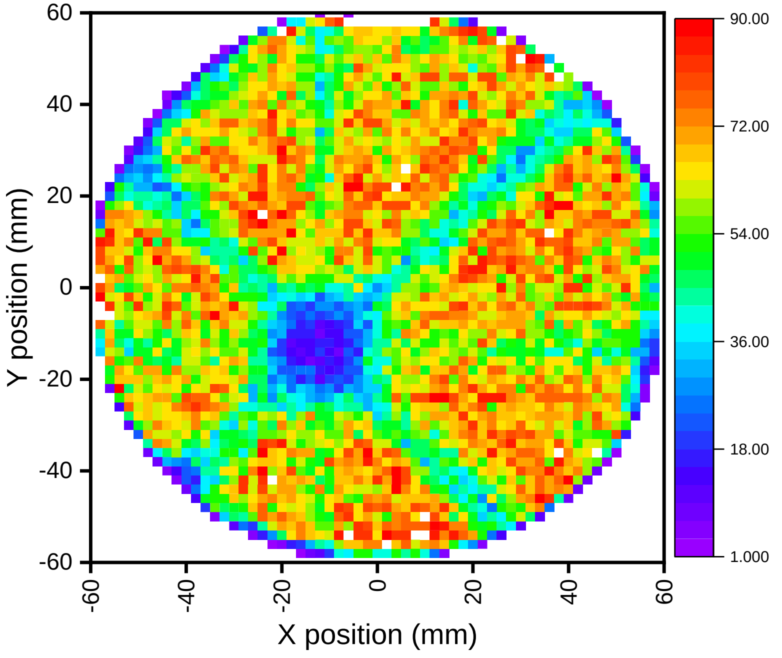

Figure 4.5: 2D Blocking pattern map of the <001> channel of a thin 50 nm V sample. The spatial dimensions in the axes correspond to an angular range of approximately 22º. Primary beam: 200 keV H_2^+

5. Correlation of optical transmittance and H concentration in Cr/V

In recent years, Fe/V and Cr/V superlattice structures have been studied in order to study the impact of the proximity effects [97]. Multilayer films of these two systems, with a nominal Fe(Cr)/V thickness ratio of 2/14, repeated 23 times, were grown prior to this dissertation and characterized extensively through transmission electron microscopy (TEM), x-ray reciprocal-space mapping and neutron scattering measurements [93,98]. For both systems, optical isotherms had also been recorded, but, in order to correlate the changes in the optical transmittance of the films with the concentration of hydrogen in them, a separate series of measurements is required. This chapter will focus on the experimental measurements that were conducted with the aim of correlating the optical changes of the Cr/V system with the hydrogen concentration. This experimental study had the following procedure: First, the superlattice was hydrogenated at an arbitrarily chosen pressure and the changes in optical transmittance were recorded for a wavelength range of 600-1000 nm. Next, the hydrogen concentration was determined using NRA, based on the $^{1}H(^{15}N,\alpha\gamma)^{12}C$ reaction. The procedure was repeated for different hydrogen concentrations, covering a wide concentration range and the resulting points were fitted with a linear function to obtain the conversion factor. The conversion factors obtained assisted in the comparison of the optical properties of the Fe/V and Cr/V systems, in a recent study [44]. All studies were conducted at the Tandem Laboratory [99], at Uppsala University and are presented in detail in Paper I [100].

5.1. Optical measurements

The optical study was conducted at the OSFOLD setup [101], which consists of a vacuum chamber that can be filled with hydrogen gas, with two windows on opposing flanges that allow light to pass through the sample. The optical measurements were carried out in a simple transmission geometry, illustrated in Figure 5.1, using the light from a polychromatic source, which produced a light beam in the wavelength range of 200 – 1000 nm. The light beam was collimated and sent through the sample, before being collected by an optical sensor. The base pressure of the chamber was in the order of 10^{-9} mbar before the introduction of the hydrogen gas. The pressure of the chamber was measured by two independent sensors. Moreover, the chamber offered annealing capabilities, with the temperature of the sample being measured using a K-type thermocouple.

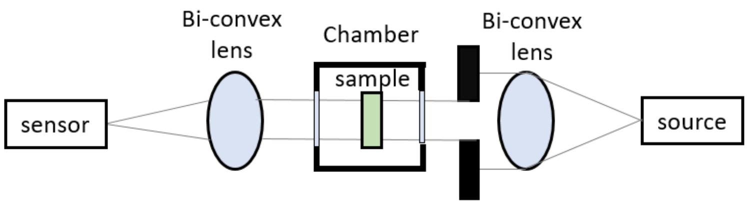

Figure 5.1: Illustration of the setup used for the optical measurements.

The experimental procedure for the optical measurements is described in detail in Paper I, but the key points will be summarized in this section. Before each loading procedure, the Cr/V sample was annealed, at UHV conditions, at a temperature of 140^{o}C and then cooled down to room temperature, namely 23^{o}C, to ensure that no hydrogen remained in the V layers from previous loadings. The optical transmittance of the sample was then recorded for wavelengths in the range of 200-1000 nm, at room temperature, to obtain a transmission spectrum representing the non-hydrogenated/pristine sample. Next, the sample was annealed to 140^{o}C and it was exposed to hydrogen gas of controlled pressure. The V layers in the Cr/V stack absorbed hydrogen, changing the optical properties of the film, which was indicated by a decrease in the intensity for all wavelengths. During the whole process the average intensity in a selected wavelength range, namely of 630-1000 nm, was recorded as an indicator of the changes in the transmittance. When optical changes were no longer observed, equilibrium was deemed to have been reached. The final step included cooling down the sample and pumping out the hydrogen gas. The optical transmittance of the hydrogenated superlattice would then be recorded again, at room temperature, to obtain a spectrum characteristic for the hydrogenated state. Afterwards, the hydrogenated sample was moved to the IBA setup.

Figure 5.2 presents characteristic transmission spectra that were obtained prior to and after the hydrogenation, along with their ratio, presented in blue points. The low intensity at lower wavelengths, resulted in higher noise-to-signal ratio in that region, which is the reason that the analysis was focused in the wavelength region above 600 nm. A major advantage of the present experimental approach is that it can provide quantitative information on how the optical properties change in different wavelength regimes, upon hydrogenation. In Figure 5.2 it can be seen clearly that the ratio is not the same for the total optical range scanned. A detailed plot with the ratios obtained for all the different loading pressures can be found in Paper I.

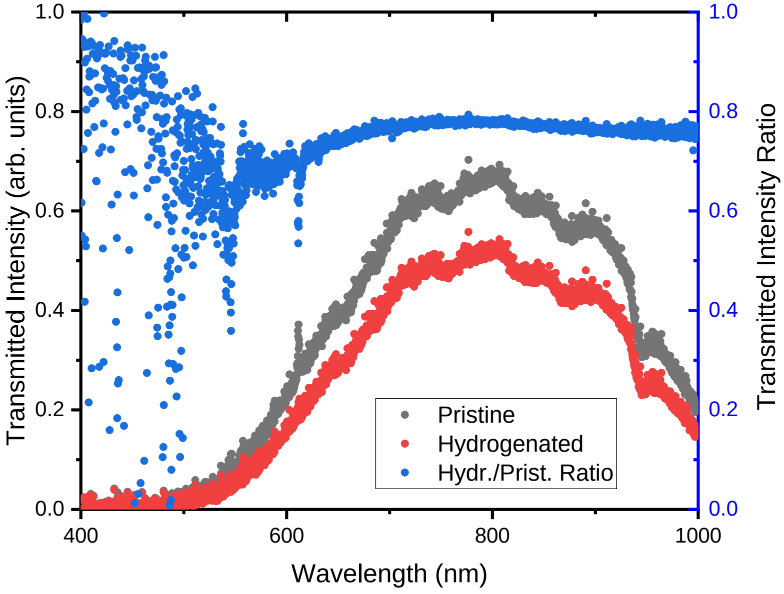

Figure 5.2: Characteristic optical transmittance spectrum for the pristine (black) and hydrogenated (red) superlattice, at a nominal pressure of 20 mbar, in the wavelength range of 400-1000 nm. The ratio of the two is indicated by the blue points.

The simultaneous cooling down of the sample and the removal of the H_2 gas from the chamber allows the quenching of the hydrogen contained in the sample. If the heating was turned off with the sample still being immersed in H_2 atmosphere, then it would absorb a high hydrogen amount and could potentially break. On the other hand, if the H_2 gas was removed while the sample was kept at high temperature, then the hydrogen in the sample would simply leak out. Therefore, it is crucial that these two processes happen simultaneously. In this stage, the Al_2O_3 capping layer plays an important role by significantly slowing down all hydrogen transport in the surface, until the sample cools down to a temperature where the thermal energy of the contained hydrogen atoms is not sufficient to overcome the potential barrier of the capping. As a result, the sample would reach room temperature while retaining most of the hydrogen that was loaded. It is vital to note that even if the amount of hydrogen was slightly altered during the cooling down process, it was not a problem for these series of measurements, because the final aim was to record pairs of optical transmittance and hydrogen concentration, in a wide concentration range.

5.2. IBA measurements

The IBA measurements took place in a scattering chamber that is electrically isolated to allow the integration of current of the incoming ^{15}N ions. The base pressure of the vacuum chamber during the measurements was in the order of 10^{-8} mbar. A simplified illustration of the setup is presented in Figure 5.3 below. A bismuth germanate (BGO) gamma detector was positioned outside of the vacuum chamber, in order to record the gamma-rays produced by the $^{1}H(^{15}N, \alpha\gamma)^{12}C$ reaction. This gamma-ray detector was also surrounded by a lead shield, in order to reduce the interactions of the detector with the natural radiation background and therefore minimize its dead-time. Additionally, the chamber was equipped with a solid-state detector, fixed at 170° with respect to the direction of the primary beam that recorded the backscattered ^{15}N particles. The setup was also equipped with a camera to assist with the alignment of the ion beam. The sample manipulator allowed for independent XYZ translational movement and rotation around the primary axis of the manipulator, denoted as X axis in Figure 5.3.

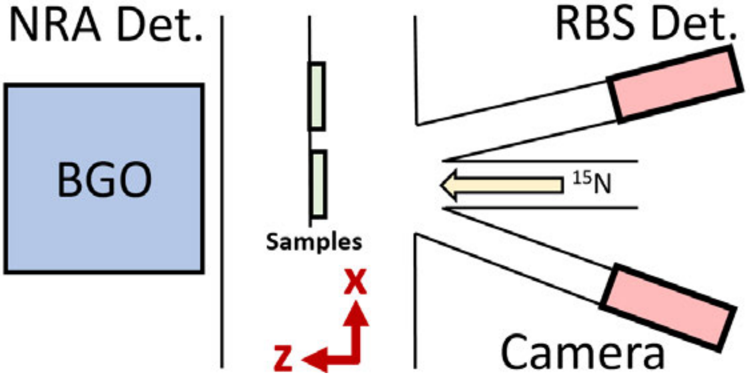

Figure 5.3: Simplified illustration of the setup for the simultaneous NRA and RBS measurements.

A gamma-ray spectrum of the hydrogenated superlattice is presented in Figure 5.4. The most pronounced peaks in the low energy regime correspond to natural radiation background from the radioactive decay of the isotopes ^{40}K and ^{208}Tl. The 4.43 MeV gamma-rays from the $^{1}H(^{15}N, \alpha\gamma)^{12}C$ reaction resulted in the presence of both a distinct peak and a low-energy tail in the spectrum. This low-energy tail corresponds to Compton scattering events of the 4.43 MeV gamma-ray with the material of the detector, resulting in only a part of the photon's energy being deposited in the detector. The events in the Compton tail still correspond to interactions of the primary ^{15}N beam with the hydrogen in the material, therefore they are included in the integration window chosen. In practice, a region of interest (ROI) starting from, approximately, an energy of 3 MeV, below of which the natural radiation peaks become pronounced, was chosen. The ROI is extended to approximately an energy of 4.75 MeV to include the main gamma peak of the $^{12}C^{*}$ deexcitation, which is broadened due to the limited energy resolution of the BGO detector. In the energy range beyond 3 MeV, the interactions of the detector with cosmic muons constitute the dominant contribution in the background of the energy spectrum. The acquisition time of a single spectrum was in the order of 200-300 sec.

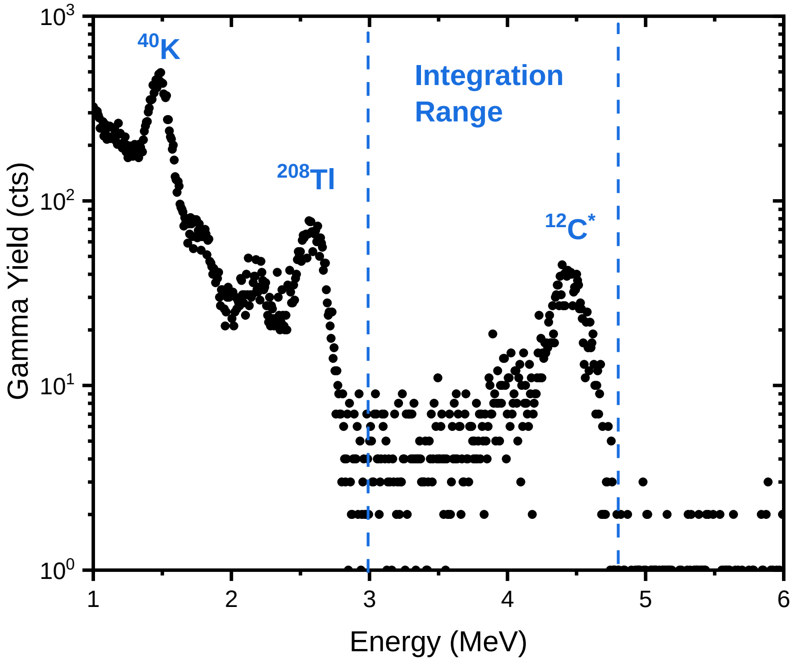

Figure 5.4 Characteristic gamma-ray spectrum from the hydrogenated Cr/V superlattice.

The first step of an IBA measurement on the Cr/V superlattice, was an angular scan to ensure that no channeling would affect the NRA scan. In general the sample was always mounted in a stage, with a 5-7º tilt and it was given an additional rotation, between 10-20º, around its surface normal, with the aim of irradiating it as close as possible to the random direction. An angular scan was then performed, typically within a range of few degrees, in order to accurately determine an orientation where the channeling effects were minimized. During the scan, the gamma-ray yield from the ROI and the backscattered V events were simultaneously recorded. Figure 5.5 presents a typical channeling pattern recorded. Based on this pattern, by giving the sample a rotation of approximately 2º, in this example, the ^{15}N irradiation was considered to be in the random direction.

The energy of the ^{15}N beam was initially set to 6.37 MeV, which was an energy below the resonance energy that always resulted in a gamma-ray spectrum with only background contributions in the ROI. Next, the energy of the beam was increased in steps of 15 keV, resulting in the resonance interaction between hydrogen atoms and ^{15}N ions occurring in an increasingly greater depth. The energy scans were terminated in an energy of, approximately, 6.7 MeV, which corresponded to the first layers of the MgO substrate that contained negligible amount of hydrogen. An additional scan in the backward direction was always performed in order to ensure that no major hydrogen loss [102] was occurring during the measurement. Figure 5.6 illustrates a typical NRA energy scan for the hydrogenated superlattice. The regions below 6.5 MeV correspond to the capping layers, namely Al_2O_3 and Pd, followed by a plateau in intensity, which corresponds to the hydrogen contained in the Cr/V layers. In order to extract the hydrogen concentration, an average of the gamma-ray yield was calculated for the 6.505-6.64 MeV range. The NRA scans for all nominal loading pressures are presented in Paper I.

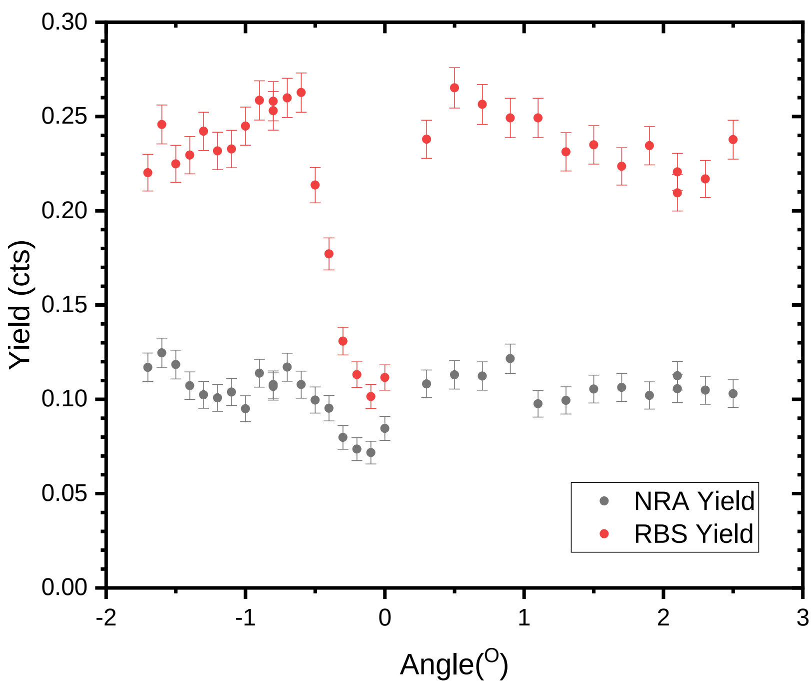

Figure 5.5 Angular scan from the hydrogenated Cr/V superlattice, using ^{15}N ions. The Y axis presents the yield per pulse from the current integrator unit.

The NRA study was a relative measurement that was based on a reference sample [103], which was a silicon (Si) wafer with an amorphized, H-implanted layer of known concentration $C_H = 18.5\%$, extending approximately 250 nm deep in the Si. This approach eliminates the dependency on physical quantities that are not easy to determine accurately, such as the solid angle and the efficiency of the detector, as well as on the exact value of the cross section and the width of the resonance. The average hydrogen concentration, expressed in at/cm^3, was obtained by:

$$n_H = \frac{Y_{Cr/V}}{Y_{ref}} \frac{N_{ref}}{N_{Cr/V}} \frac{S_{Cr/V}}{S_{ref}} n_{ref} \quad (5.1)$$

in which, *Y* denotes the gamma yield, *N* is the total number of atoms that reached the sample, *S* the stopping power of the hydrogenated layers and n_{ref} denotes the atomic concentration, in atoms/cm^3, in the reference sample. Equation 5.1 was used in an iterative approach, where an initial stopping power value S_0 was used to extract an atomic hydrogen concentration n_0, which was afterwards used to extract the stopping power *S* for the next iteration, using the SRIM code. The full details on the iterative procedure can be found in Paper I.

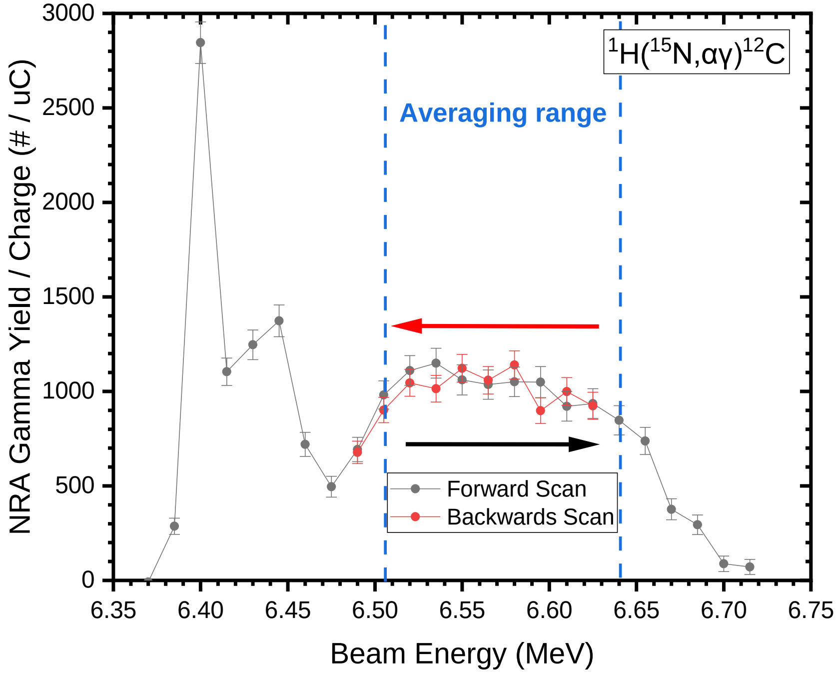

Figure 5.6 Characteristic NRA energy scan from the hydrogenated Cr/V superlattice. Part of the scan was repeated in the backwards direction, indicated by red points, in order to ensure that no hydrogen losses occurred during the irradiation.

5.3. Correlation of NRA and optical measurements

The different pairs of hydrogen concentration and optical transmittance values are presented in Figure 5.7. A total of six loadings took place during the study, covering a wide range of hydrogen concentrations, expressed in H/V ratio. For each loading the optical changes were extracted for different wavelengths regimes, namely 600, 700, 800, 900 and 1000 nm and all revealed a linear relationship between the optical changes and the H concentration. Moreover, a linear fit was performed to the data for each wavelength, in order to extract the conversion factor. The results of the fit are presented in Table 5.1, revealing a stable slope on the wavelength range of 700-1000 nm, but an increase in slope for wavelengths near 600 nm, which confirmed a wavelength dependence on the changes in the optical properties. A minor positive offset was also observed in the fitted curves, which was attributed to a minor drift in the intensity of the light source, which resulted in a slightly increased recorded intensity drop in the optical transmittance.

Table 5.1 Results of the linear fitting procedure in different wavelength ranges.

Wavelength (nm)	Slope	Intercept
600±5	0.86±0.05	0.014±0.004
700±5	0.64±0.03	0.015±0.002
800±5	0.60±0.03	0.022±0.004
900±5	0.65±0.03	0.018±0.003
1000±5	0.65±0.04	0.021±0.003

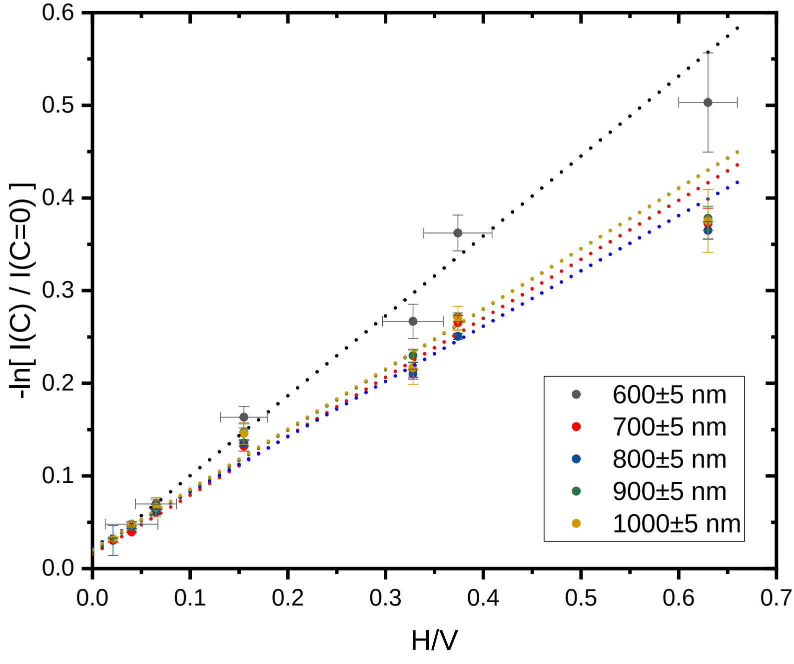

Figure 5.7 Correlation of the optical transmittance and the hydrogen concentration, at room temperature for different wavelength regimes in the range of 600-1000 nm.

6. Towards an in-situ setup

The present experimental approach, which involved the ex-situ formation of hydrides and the subsequent analysis of their concentration through NRA, is characterized by some inherent limitations. The consequences of using this hydrogen quenching procedure and other effects such as the hydrogen loss during the irradiation, will be discussed in this chapter. Furthermore, a potential solution for all the aforementioned issues, will be presented, in the form of an in-situ gas-cell, which will allow the hydride formation and the IBA to occur in the same setup. In the sections below, the practical constraints in terms of pressure and temperature range for such studies, as well as the potential limitations of the proposed setup will be discussed, along with the results of complementary theoretical and experimental studies. A more extended description of the aforementioned points can be found in paper II.

6.1. Present limitations

The IBA techniques allow for quantification of the hydrogen concentration and extraction of real-space information on the interstitial location at room temperature or at cryogenic temperature ranges [104], but measurements with the sample being in high temperature are prohibited due to the thermal hydrogen losses. Since the IBA measurements are carried out in UHV, if a hydride was to be exposed to high temperatures, the contained hydrogen would obtain enough thermal energy to overcome the surface barriers and be released from the V layers. The hydrogen quenching procedure followed in the previous chapter can allow one to partially overcome this issue by loading a sample with a range of hydrogen concentrations that could not be achieved in room temperature and then trapping the hydrogen in the V using the oxide layer. This approach is indeed rigid in the context of some studies, such as correlating H concentration to physical properties such as optical transmittance that was presented in Chapter 5. However, the potential addition or removal of hydrogen during the cooling down stage means that it is no longer possible to correlate the amount of hydrogen measured with NRA with the pressure and temperature used during the loading.

Even by employing the hydrogen quenching procedure, which was described in the previous chapter, and conducting the IBA measurements at room temperature, there is an additional limitation originating from the use of an ion beam as a probing tool. The sample can experience irradiation-induced hydrogen losses [102], referred to as H-losses in the following text, that result in the alteration of the hydrogen concentration profile during the profiling measurement. Estimating the H-loss rate can be challenging and any corrections applied during the data analysis stage will, inevitably, introduce additional uncertainties. In practice, in order to limit the H-losses one must restrict the beam intensity, which refers to the power delivered per unit area. It is achieved by deliberately defocusing the ion beam, to cover a larger area, as well as reducing the value of its current. Furthermore, the presence of the Al_2O_3 capping layer plays a vital role in reducing the hydrogen losses, due to its ability to act as a barrier for the hydrogen bound in the V. In fact, when measurements took place without this capping layer, H-loss was observed even after having minimized the ^{15}N intensity. However, the reduction of current results in a lower NRA yield, which corresponds to a higher signal-to-background ratio and leads to longer measurement times, if one wishes to retain the precision of the measurement. Moreover, this approach forbids the study of samples with a smaller area, for example in the order of 5x5 mm^2, since a part of the ion beam would most likely irradiate the sample holder and affect the gamma-ray yield recorded.

Figure 6.1 illustrates an example of H-losses that occurred in a measurement of the hydrogenated Cr/V superlattice. The plot excludes the energy range corresponding to the surface, for a better showcasing of the H-loss effect. In this particular case, the loss occurred due to the ^{15}N beam being focused to an area of few mm^2, in contrast to the 20-30 mm^2 area that was commonly irradiated in that series of experiments. The duration of the spectrum acquisition was 200 sec and the backwards scan, revealed the H-losses. By focusing on the two data points on 6.595 MeV, which were recorded approximately 45 minutes apart, a reduction of approximately 40% can be observed. It is important to note that, given the H-losses, the forward direction scan recorded in this case also does not correspond to the initial hydrogen depth distribution in the superlattice, since the hydrogen inventory in the V layers was being reduced as the capping layers were scanned. The NRA scan of the complete energy range is presented in Paper II. In the presented measurement the value of the beam current, was restricted below 1.5 nA and losses were still clearly observed.

6.2. Design of an in-situ gas-cell

Our proposed approach for overcoming the aforementioned limitations, is to combine the hydrogenation setup with the IBA setup. The key concept, based on which this new in-situ IBA setup was designed, involves keeping a thin metal hydride film continuously immersed in a gaseous H_2 atmosphere, while it is irradiated with ^{15}N ions. The advantages are numerous: First of all, the sample can be in gaseous atmosphere at a temperature beyond room temperature, permitting measurements in thermal equilibrium without losses. In fact, any hydrogen loss that occurred, would immediately trigger a hydrogen exchange between the gas and the metal hydride to restore the equilibrium H concentration in the latter. For the same reason, the issue of ion-induced H-losses would also be solved, as the sample would continuously attempt to thermally equilibrate with its gaseous environment, thus recovering any lost hydrogen due to the irradiation. Moreover, the kinetics of this exchange could be accelerated by the removal of the Al_2O_3 capping layer to allow the direct contact of the H_2 gas with the Pd layer that catalyzes the dissociation of H_2. Finally, the quenching process that was described in the previous chapter is no longer needed in this in-situ approach. By controlling the pressure and temperature of the surrounding H_2 gas a wider range of loading concentrations are accessible in this configuration. A detailed technical drawing, along with the corresponding description of the design can be found in Paper II.

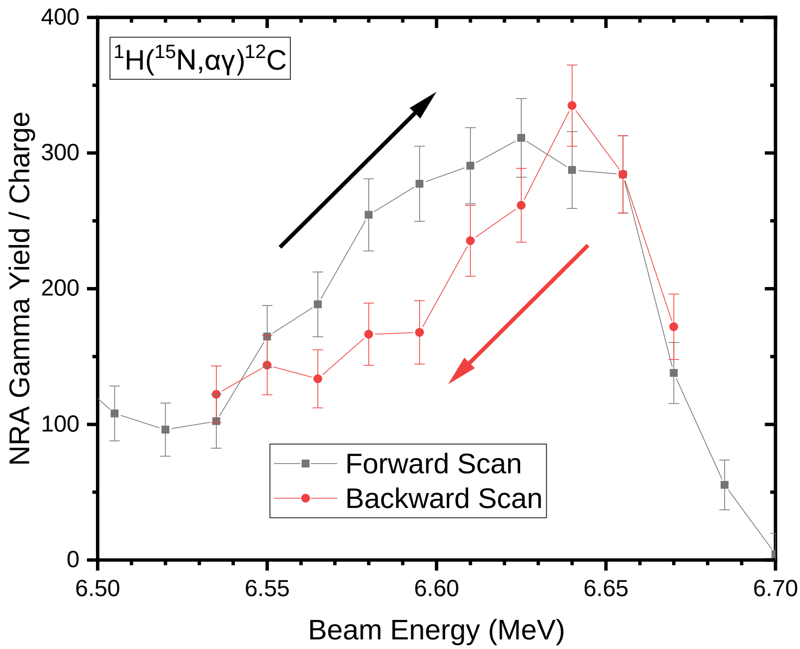

Figure 6.1: Gamma excitation function of $MgO/CrV/Pd/Al_2O_3$ hydrogenated superlattice, using the $^1H(^{15}N,\alpha\gamma)^{12}C$ resonant reaction.

The gas-cell is designed to be integrated in a commercial sample holder, which will be responsible for the translational motion in the three major Cartesian axes and two independent rotations. The choice of the sample holder aims to correct for the offset between the plane of the surface of the sample is on and the plane of the holder. The gas-cell is comprised of two parts, a main-body and a lid, with the total volume occupied being in the order of 40 cm^3. The proposed material of construction is high purity aluminum (Al), because it allows the part to be light-weight, meaning that it can be easily rotated by the commercial holder with the minimum strain in the rotation mechanisms. Moreover, the backscattering signal from a low-Z element such as Al would not interfere with RBS spectra from transition metals such as V, if a part of the beam intensity was irradiating the gas-cell. Finally, the effect of embrittlement [63] due to the presence of H is also less pronounced in Al, compared to stainless steel.

Allowing IBA measurements of metal hydrides in high temperatures is a major advantage of this system, thus it is important to consider the upper limits of the working temperature range. The choice of the Al as the primary material will be accompanied by the choice of an O-ring sealing, which is indicates that the temperature of the current setup should not exceed, under normal circumstances, 210 ^oC. It should be noted however that the vacuum sealing can still be maintained during an intermittent heating beyond 210 ^oC, but it will severely reduce the lifetime of the seal. The heating process can be automated through the use of temperature controller connected to a heating sensor and a resistance heater. Moreover, in order to achieve a precise control of the temperature, both of these elements are designed to be in direct thermal contact with in the main body of the gas-cell. Both the heating and sensor elements selected have a thin oxide coating, to insulate them electrically, that way the main body can also collect the current of the primary ion beam for charge normalization purposes. An electrical bias can also be applied, to the isolated part, to suppress any secondary electron emission.

The O-ring sealing between the main body and the lid, creates a low-volume, enclosed space which will accommodate the H_2 gas, in the order of few cm^3. A detailed description of the gas piping system is given in Paper II, but the main principle is that the H_2 gas is transferred from the outside of the chamber, through a stainless-steel bellow and is then sealed in the part. The lid is designed to accommodate both the sample and the membrane window, while minimizing the distance between the membrane and the surface of the sample and therefore the path of the incoming ions through the gas cloud, below 1 mm. The details on the sample mounting can be found in paper II. Finally, a silicon-rich nitride (SiRN) window is needed to simultaneously retain a vacuum sealing but also allow the ^{15}N ion beam to reach the sample. The maximum pressure to be reached is in the order of 1 bar, in contrast to setups based on differential pumping [105], which can achieve maximum pressures in the order of 1 mbar.

6.3. Theoretical and experimental results on ^{15}N ions through SiRN

The SiRN membrane will interact with the ^{15}N ions before they reach the surface of the sample, reducing their energy and widening the distribution of their energies, due to the effect of energy straggling. Additionally, a geometrical divergence of the primary ions from the straight trajectory is also expected, which will prevent some of these ions from being steered in a channel even if the ion beam is aligned with a crystallographic axis. In order to quantify such effects, the trajectories of ^{15}N ions, with a kinetic energy of 6.4 MeV, were simulated using the TRIM code. In the simulation, a two-layer structure was created, which included an initial layer of silicon-rich nitride and a second layer of H_2 gas. In the first layer, the N/Si ratio was set to 1.1 and the density to 3 g/cm^3, as suggested by the manufacturer. It should be noted that experimental results have reported density values for the silicon nitride layer that are 20% lower from the suggested value [106], so the presented results will indicate an upper limit. The result of the simulation includes the final energy and direction of each simulated ion that exits the two-layer structure. With satisfactory statistics, namely in the order of 250.000 events, the energy distribution of the ions can be clearly defined, as seen in Figure 6.2.

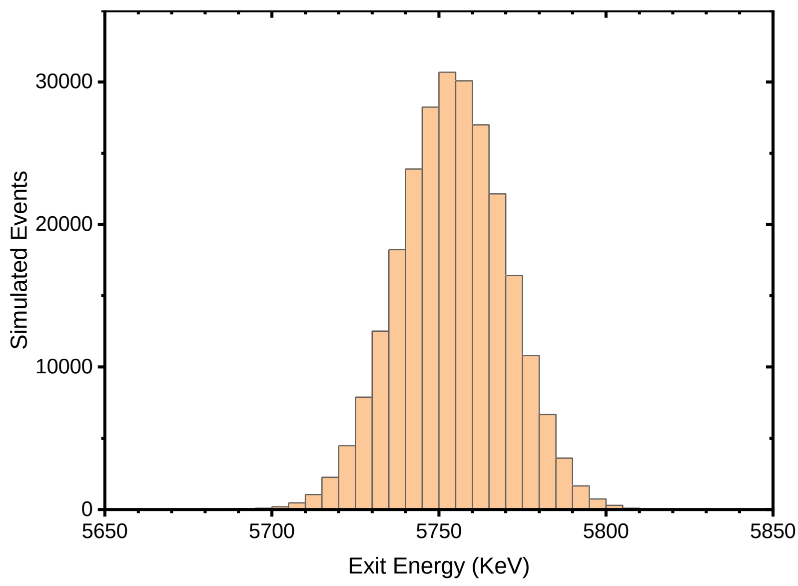

Figure 6.2: Simulated angular distribution of 6.4 MeV ^{15}N ions through a 100 nm SiRN layer and 1 mm gas H_2. Number of simulated events: 250.000.

The exiting direction of each simulated projectile is provided in the form of the three directional cosines, which, allows for the calculation of the angular divergence of each simulated ion and therefore their angular distribution, after passing through these layers. It should be noted that in a simulation using the TRIM software the x axis, characterized by the (100) vector, represents the axis of the primary beam. Figure 6.3 illustrates the distribution for a SiRN layer of 100 nm and 1 mm of H_2 gas.

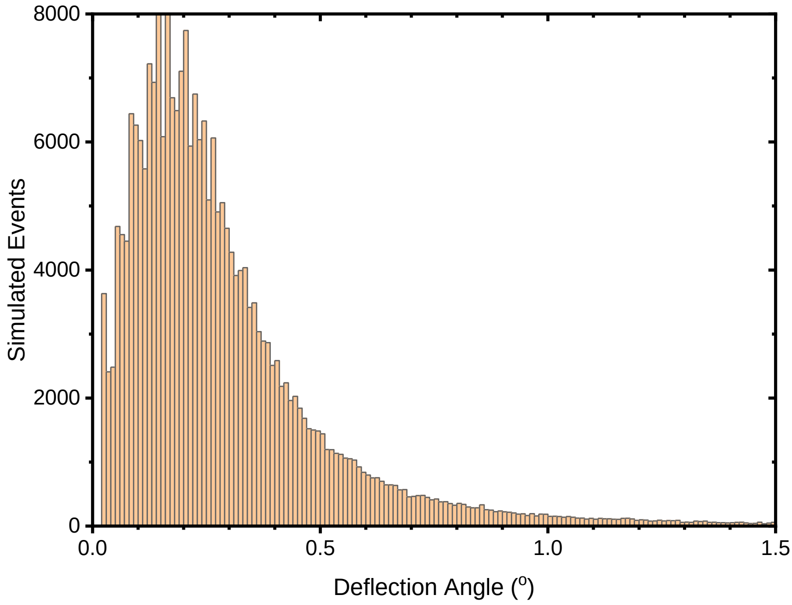

Figure 6.3: Simulated angular distribution of 6.4 MeV ^{15}N ions through a 100 nm SiRN layer and 1 mm gas H_2 (Pressure: 1 bar), Number of simulated events: 250.000.

Simulations were run for different combinations of the thicknesses of the two layers. Figure 6.4 showcases a series of runs where the thickness of nitride layer was fixed to 150 nm and the thickness the H_2 layer was varied in the range of 0.5 - 4 mm. This SiRN thickness corresponds to a window that can withstand a pressure difference of 1 bar, so it was chosen to showcase the relative contribution of the two layers to the beam divergence. As seen in Figure 6.4, the angular distributions of the ^{15}N ions produced by the simulation for H_2 gas layer, corresponding to a pressure of 1 bar, and a thickness in the range of 0.5 - 4mm present negligible difference. Moreover, by considering that many experiments will be carried out at a lower pressure regime, namely 0.1-10 mbar, the straggling effect produced by the gas will be insignificant compared to that produced by the membrane. Based on this result, a follow-up series of simulations was run, with the thickness of the H_2 layer fixed to 1 mm and the thickness of the nitride layer being varied in the range of 30-200 nm. The results are discussed in detail in Paper II.

To validate the simulation results, which showed the thickness of the SiRN to be the dominant factor in defining energy and angular straggling, an experimental study was carried out. For this purpose, a new series of experimental measurements was conducted, with a sample configuration as follows: A SiRN, with a thickness of 150 nm was fixed on top of the reference Si-H sample and an NRA energy scan was carried out. The obtained excitation function is presented in Figure 6.5, where the range up to 6.65 MeV corresponds to the hydrogen content of the membrane itself, followed by the homogeneous H distribution. This offers a first look on the characteristic traits that all NRA measurements will have on the designed setup. Furthermore, the H content on the window surface can be used for accelerator calibration purposes to calculate the offset between the nominal and the real energy of the ^{15}N ions.

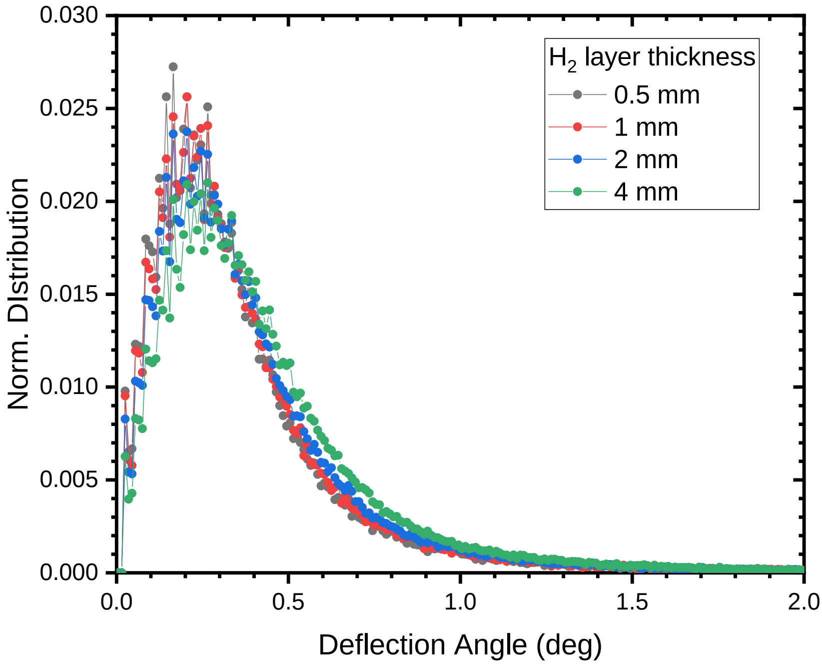

Figure 6.4. Angular distribution of simulated 6.4 MeV ^{15}N ions, after passing through a 150 nm SiRN membrane and a H_2 gas layer (Pressure: 1 bar) of varying thickness.

A similar experiment was conducted with a hydrogenated Cr/V superlattice. The corresponding NRA energy scan yielded a similar excitation function, which is presented in Paper II.

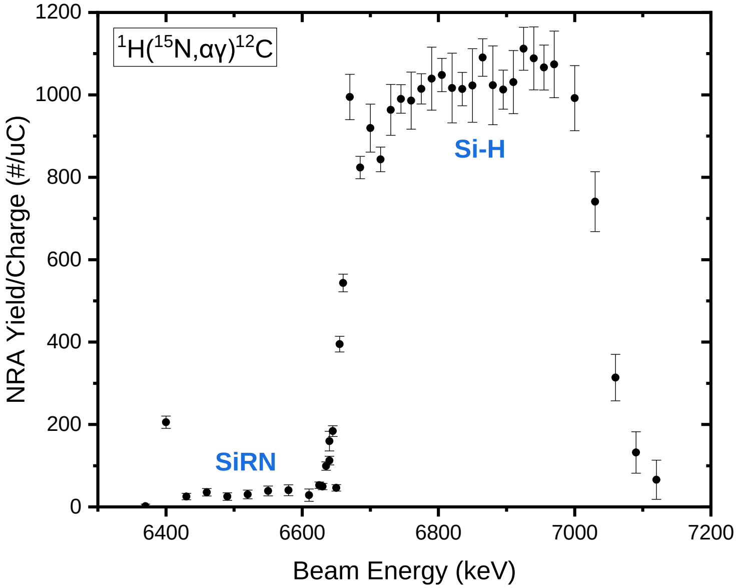

Figure 6.5: Excitation function of an amorphized Si-H irradiated with ^{15}N ions through a SIRN membrane, with a thickness of 150 nm.

Afterwards, an angular scan was conducted, over an angular range of 6^{o}, in order to search for channeling patterns. Figure 6.6 presents a recorded planar channeling pattern, which proves that even for a membrane of 150 nm thickness it is still possible to obtain real-space crystallographic data. It should be noted that this particular membrane thickness is expected to be able to withstand a pressure gradient of 1 bar. This experimental result is in agreement with the theoretical simulations, presented in Paper II, which predicted that a large percentage of the ^{15}N ions will be able to remain in a trajectory that will allow them to be channeled, after passing through the SiRN membrane. A more detailed analysis on the obtained pattern is included in paper II.

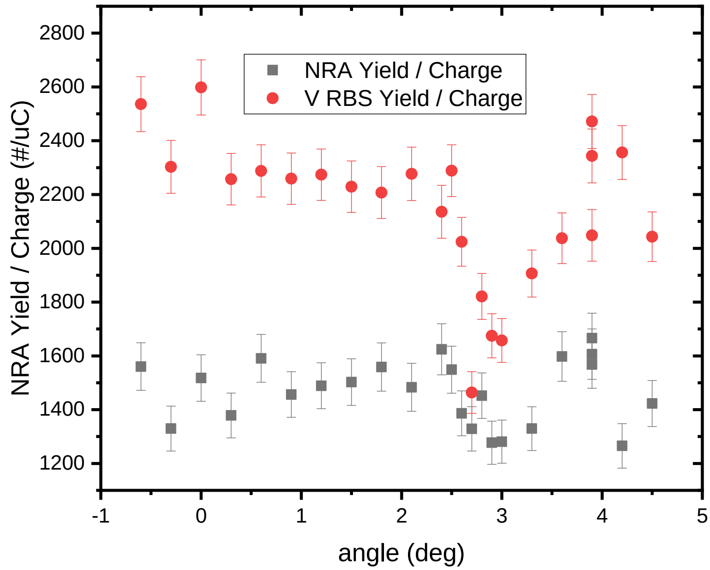

Figure 6.6. Excitation function of a hydrogenated Cr/V superlattice, irradiated with ^{15}N ions through a SiRN membrane, with a thickness of 150 nm.

7. Conclusions and Outlook

Metal hydrides have been studied for many years for hydrogen storage purposes, but, in order to engineer storage materials with improved thermodynamic properties, the effects of finite size, strain and proximity of foreign atom species need to be fully understood. This work has focused on the utilization of IBA techniques, as well as complementary optical and x-ray techniques, in order to study different aspects of the vanadium hydride system.

First, as a part of this work, the growth process of thin V films, in a thickness range of 20-80 nm was optimized, through x-ray measurements. Improving the quality of samples is an important step, with the samples grown during this dissertation being included in different projects that were studying the VH system. Moreover, during this work, the growth conditions and thicknesses of the Pd & Al_2O_3 capping layers was reviewed, with sub-nm Pd layers yielding the blocking patterns with high channelling intensity contrast, using ToF-MEIS.

Taking a step further in the study of V-based systems, this work has examined superlattice structures. Understanding the proximity effects in the Fe/V and Cr/V systems featuring similar strain profiles from existing optical isotherm data required a conversion factor between optical transmittance changes and hydrogen concentration. For this reason, the Cr/V system was studied in order to correlate the changes optical transmittance upon hydrogenation to the concentration of hydrogen in the V layers. The study was conducted over a wavelength range of 600 - 1000 nm. A linear relationship was revealed in all wavelengths, with the range of 700 - 1000 nm, showing negligible wavelength dependence, in contrast to the 600 - 700 nm range. This effect was attributed to the wavelength dependence of the dielectric function of the system.

While studying both the V and the Cr/V systems, some limitations of the IBA techniques were highlighted. The capabilities of the IBA techniques include quantitative extraction of a depth profiling of the hydrogen concentration, as well as of real-space crystallographic information. However, the H-loss effect can create problems in room temperature measurements and the thermal desorption forbids the studies at high temperatures. In order to overcome these limitations, a design for a system allowing in-situ and in-operando IBA studies on metal hydrides, immersed in H_2 gas, was proposed. This approach involves an electrically-isolated gas-cell, with controlled temperature up to 210°C. The transition from the UHV environment of the scattering chamber to a gaseous H_2 atmosphere of up to 1 bar, which is inside the gas-cell, is possible through a SiRN window. The effect of this window in the energy and trajectory of the primary ^{15}N ions used for NRA and planar channeling measurements was quantified with theoretical simulations and experimental studies. The NRA scans showcased the characteristics of the excitation functions that can be expected, as well as some information on the H-content and energy loss on the SiRN membranes themselves. Planar channeling patterns were also revealed, providing a proof of principle for channeling measurements with the proposed setup.

Extending the capabilities of the IBA techniques with improved infrastructure will allow the direct probing of more phases in the phase diagram of hydride systems based on elements such as V and Pd. Furthermore, it will allow cross-checking with the thermodynamic data that currently exists in the literature, from studies that employed reciprocal space techniques or chemical techniques.

Acknowledgements

I would like to thank everyone that helped and supported me in this two-year journey at Uppsala University.

First and foremost, I would like to express my gratitude to my primary supervisor, Daniel Primetzhofer, for the guidance he provided during all stages of the dissertation. Next, I would like to thank my co-supervisor Max Wolff for his support and for his precious scientific input in the projects that I was a part of. Moreover, I would also like to thank my third supervisor, Robert J. W. Frost, for his support at the technical design aspects of my work, as well as for all the encouragement he provided over those two years. Finally, I would like to extend my thanks to my final supervisor Gunnar K. Pálsson, for all the discussions on the field of hydrogen storage.

Furthermore, I would like to thank from my heart my seniors Kristina and Dmitrii for their guidance and patience, while showing me the ropes in a scientific field that was new to me. I offer special thanks to my colleagues Radek and Felipe for our collaborations and for making the workspace a better place. I extend my thanks to all my colleagues in the ion physics group, namely: Rajdeep, Jila, Gyula, Ghada, Eleni, Philipp, Tuan, Petter and Eduardo for creating the nice professional and educational environment that I was lucky to be part of. Of course none of it would be possible without my colleagues at Tandem Lab. I thank our engineers Bart, Sven, Mauricio and Johan for their support on the technical issues that occurred and Svenja, our communications officer, for her support during the publishing of the thesis.

Finally, I thank my friends and family for being on my side during these years.

References

[1] T. Ahmad, D. Zhang, A critical review of comparative global historical energy consumption and future demand: The story told so far, Energy Reports 6 (2020) 1973–1991. https://doi.org/10.1016/j.egyr.2020.07.020.
[2] A. Züttel, A. Remhof, A. Borgschulte, O. Friedrichs, Hydrogen: the future energy carrier, Phil. Trans. R. Soc. A. 368 (2010) 3329–3342. https://doi.org/10.1098/rsta.2010.0113.
[3] M. Höök, X. Tang, Depletion of fossil fuels and anthropogenic climate change—A review, Energy Policy 52 (2013) 797–809. https://doi.org/10.1016/j.enpol.2012.10.046.
[4] D. Gielen, F. Boshell, D. Saygin, M.D. Bazilian, N. Wagner, R. Gorini, The role of renewable energy in the global energy transformation, Energy Strategy Reviews 24 (2019) 38–50. https://doi.org/10.1016/j.esr.2019.01.006.
[5] N. Abas, A. Kalair, N. Khan, Review of fossil fuels and future energy technologies, Futures 69 (2015) 31–49. https://doi.org/10.1016/j.futures.2015.03.003.
[6] J.O. Abe, A.P.I. Popoola, E. Ajenifuja, O.M. Popoola, Hydrogen energy, economy and storage: Review and recommendation, International Journal of Hydrogen Energy 44 (2019) 15072–15086. https://doi.org/10.1016/j.ijhydene.2019.04.068.
[7] G. Marbán, T. Valdés-Solís, Towards the hydrogen economy?, International Journal of Hydrogen Energy 32 (2007) 1625–1637. https://doi.org/10.1016/j.ijhydene.2006.12.017.
[8] J.O.M. Bockris, The hydrogen economy: Its history, International Journal of Hydrogen Energy 38 (2013) 2579–2588. https://doi.org/10.1016/j.ijhydene.2012.12.026.
[9] S. Verhelst, T. Wallner, Hydrogen-fueled internal combustion engines, Progress in Energy and Combustion Science 35 (2009) 490–527. https://doi.org/10.1016/j.pecs.2009.08.001.
[10] Y. Manoharan, S.E. Hosseini, B. Butler, H. Alzhahrani, B.T.F. Senior, T. Ashuri, J. Krohn, Hydrogen Fuel Cell Vehicles; Current Status and Future Prospect, Applied Sciences 9 (2019) 2296. https://doi.org/10.3390/app9112296.

[11] S.Y. Gómez, D. Hotza, Current developments in reversible solid oxide fuel cells, Renewable and Sustainable Energy Reviews 61 (2016) 155–174. https://doi.org/10.1016/j.rser.2016.03.005.
[12] G. Halpert, H. Frank, S. Surampudi, Batteries and Fuel Cells in Space, Electrochem. Soc. Interface 8 (1999) 25–30. https://doi.org/10.1149/2.F06993IF.
[13] T. Yoshida, K. Kojima, Toyota MIRAI Fuel Cell Vehicle and Progress Toward a Future Hydrogen Society, Interface Magazine 24 (2015) 45–49. https://doi.org/10.1149/2.F03152if.
[14] L. Schlapbach, A. Züttel, Hydrogen-storage materials for mobile applications, Nature 414 (2001) 353–358. https://doi.org/10.1038/35104634.
[15] F. Dawood, M. Anda, G.M. Shafiullah, Hydrogen production for energy: An overview, International Journal of Hydrogen Energy 45 (2020) 3847–3869. https://doi.org/10.1016/j.ijhydene.2019.12.059.
[16] A. Züttel, Hydrogen storage methods, Naturwissenschaften 91 (2004) 157–172. https://doi.org/10.1007/s00114-004-0516-x.
[17] S. Anwar, F. Khan, Y. Zhang, A. Djire, Recent development in electrocatalysts for hydrogen production through water electrolysis, International Journal of Hydrogen Energy 46 (2021) 32284–32317. https://doi.org/10.1016/j.ijhydene.2021.06.191.
[18] M.H. Sellami, K. Loudiyi, Electrolytes behavior during hydrogen production by solar energy, Renewable and Sustainable Energy Reviews 70 (2017) 1331–1335. https://doi.org/10.1016/j.rser.2016.12.034.
[19] J. Incer-Valverde, A. Korayem, G. Tsatsaronis, T. Morosuk, “Colors” of hydrogen: Definitions and carbon intensity, Energy Conversion and Management 291 (2023) 117294. https://doi.org/10.1016/j.enconman.2023.117294.
[20] M. Yadav, Q. Xu, Liquid-phase chemical hydrogen storage materials, Energy Environ. Sci. 5 (2012) 9698. https://doi.org/10.1039/c2ee22937d.
[21] A.M. Elberry, J. Thakur, A. Santasalo-Aarnio, M. Larmi, Large-scale compressed hydrogen storage as part of renewable electricity storage systems, International Journal of Hydrogen Energy 46 (2021) 15671–15690. https://doi.org/10.1016/j.ijhydene.2021.02.080.
[22] J. Andersson, S. Grönkvist, Large-scale storage of hydrogen, International Journal of Hydrogen Energy 44 (2019) 11901–11919. https://doi.org/10.1016/j.ijhydene.2019.03.063.
[23] U. Eberle, M. Felderhoff, F. Schüth, Chemical and Physical Solutions for Hydrogen Storage, Angew Chem Int Ed 48 (2009) 6608–6630. https://doi.org/10.1002/anie.200806293.
[24] G. Valenti, Hydrogen liquefaction and liquid hydrogen storage, in: Compendium of Hydrogen Energy, Elsevier, 2016: pp. 27–51. https://doi.org/10.1016/B978-1-78242-362-1.00002-X.
[25] A. Züttel, Materials for hydrogen storage, Materials Today 6 (2003) 24–33. https://doi.org/10.1016/S1369-7021(03)00922-2.

[26] H.T. Hwang, A. Varma, Hydrogen storage for fuel cell vehicles, Current Opinion in Chemical Engineering 5 (2014) 42–48. https://doi.org/10.1016/j.coche.2014.04.004.
[27] Q. Li, Y. Lu, Q. Luo, X. Yang, Y. Yang, J. Tan, Z. Dong, J. Dang, J. Li, Y. Chen, B. Jiang, S. Sun, F. Pan, Thermodynamics and kinetics of hydriding and dehydriding reactions in Mg-based hydrogen storage materials, Journal of Magnesium and Alloys 9 (2021) 1922–1941. https://doi.org/10.1016/j.jma.2021.10.002.
[28] B. Sakintuna, F. Lamaridarkrim, M. Hirscher, Metal hydride materials for solid hydrogen storage: A review☆, International Journal of Hydrogen Energy 32 (2007) 1121–1140. https://doi.org/10.1016/j.ijhydene.2006.11.022.
[29] H. Sugimoto, Y. Fukai, Theory of light interstitials in bcc metals. I. Self-trapped state of hydrogen and muons in Nb, Phys. Rev. B 22 (1980) 670–680. https://doi.org/10.1103/PhysRevB.22.670.
[30] S. Kumar, A. Jain, T. Ichikawa, Y. Kojima, G.K. Dey, Development of vanadium based hydrogen storage material: A review, Renewable and Sustainable Energy Reviews 72 (2017) 791–800. https://doi.org/10.1016/j.rser.2017.01.063.
[31] J. Völkl, G. Alefeld, Diffusion of hydrogen in metals, in: G. Alefeld, J. Völkl (Eds.), Hydrogen in Metals I, Springer Berlin Heidelberg, Berlin, Heidelberg, 1978: pp. 321–348. https://doi.org/10.1007/3540087052_51.
[32] P. Kofstad, W.E. Wallace, Vapor Pressure Studies of the Vanadium-Hydrogen System and Thermodynamics of Formation of Vanadium-Hydrogen Solid Solutions [1], J. Am. Chem. Soc. 81 (1959) 5019–5022. https://doi.org/10.1021/ja01528a002.
[33] A.J. Maeland, Investigation of the Vanadium—Hydrogen System by X-Ray Diffraction Techniques [1,2], J. Phys. Chem. 68 (1964) 2197–2200. https://doi.org/10.1021/j100790a028.
[34] E. Veleckis, R.K. Edwards, Thermodynamic properties in the systems vanadium-hydrogen, niobium-hydrogen, and tantalum-hydrogen, J. Phys. Chem. 73 (1969) 683–692. https://doi.org/10.1021/j100723a033.
[35] R. Griffiths, J.A. Pryde, A. Righini-Brand, Phase diagram and thermodynamic data for the hydrogen/vanadium system, J. Chem. Soc., Faraday Trans. 1 68 (1972) 2344. https://doi.org/10.1039/f19726802344.
[36] M.V. Lototsky, V.A. Yartys, I.Yu. Zavaliy, Vanadium-based BCC alloys: phase-structural characteristics and hydrogen sorption properties, Journal of Alloys and Compounds 404–406 (2005) 421–426. https://doi.org/10.1016/j.jallcom.2005.01.139.
[37] H. Yukawa, M. Takagi, A. Teshima, M. Morinaga, Alloying effects on the stability of vanadium hydrides, Journal of Alloys and Compounds 330–332 (2002) 105–109. https://doi.org/10.1016/S0925-8388(01)01526-2.

[38] X. Xin, G.K. Pálsson, M. Wolff, B. Hjörvarsson, Finite-Size Effects: Hydrogen in Fe / V (001) Superlattices, Phys. Rev. Lett. 113 (2014) 046103. https://doi.org/10.1103/PhysRevLett.113.046103.
[39] S. Olsson, B. Hjörvarsson, Effect of biaxial elastic constraints on H − H interactions in ultrathin vanadium, Phys. Rev. B 71 (2005) 035414. https://doi.org/10.1103/PhysRevB.71.035414.
[40] R. Johansson, R. Ahuja, O. Eriksson, B. Hjörvarsson, R.H. Scheicher, Effect of uniaxial strain on the site occupancy of hydrogen in vanadium from density-functional calculations, Sci Rep 5 (2015) 10301. https://doi.org/10.1038/srep10301.
[41] H. Zabel, H. Peisl, Sample-Shape-Dependent Phase Transition of Hydrogen in Niobium, Phys. Rev. Lett. 42 (1979) 511–514. https://doi.org/10.1103/PhysRevLett.42.511.
[42] G. Alefeld, Ber. Bunsenges., Phase Transitions of Hydrogen in Metals due to Elastic Interaction, Berichte Der Bunsengesellschaft Für Physikalische Chemie 76 (1972) 746–755.
[43] G.K. Pálsson, A.K. Eriksson, M. Amft, X. Xin, A. Liebig, S. Ólafsson, B. Hjörvarsson, Proximity effects on H absorption in ultrathin V layers, Phys. Rev. B 90 (2014) 045420. https://doi.org/10.1103/PhysRevB.90.045420.
[44] K. Komander, Nanoscale Metal Hydrides from MeV-Ion Perspectives: A Unique View, Acta Universitatis Upsaliensis, Uppsala, 2024.
[45] B. Hjörvarsson, G. Andersson, E. Karlsson, Metallic superlattices: quasi two-dimensional playground for hydrogen, Journal of Alloys and Compounds 253–254 (1997) 51–57. https://doi.org/10.1016/S0925-8388(96)02941-6.
[46] J.N. Huiberts, R. Griessen, J.H. Rector, R.J. Wijngaarden, J.P. Dekker, D.G. De Groot, N.J. Koeman, Yttrium and lanthanum hydride films with switchable optical properties, Nature 380 (1996) 231–234. https://doi.org/10.1038/380231a0.
[47] R. Gremaud, C.P. Broedersz, D.M. Borsa, A. Borgschulte, P. Mauron, H. Schreuders, J.H. Rector, B. Dam, R. Griessen, Hydrogenography: An Optical Combinatorial Method To Find New Light-Weight Hydrogen-Storage Materials, Advanced Materials 19 (2007) 2813–2817. https://doi.org/10.1002/adma.200602560.
[48] J. Prinz, G.K. Pálsson, P.T. Korelis, B. Hjörvarsson, Combined light and electron scattering for exploring hydrogen in thin metallic films, Applied Physics Letters 97 (2010) 251910. https://doi.org/10.1063/1.3529465.
[49] G.K. Pálsson, A.R. Rennie, B. Hjörvarsson, Examination of the reliability of x-ray techniques for determining hydrogen-induced volume changes, Phys. Rev. B 78 (2008) 104118. https://doi.org/10.1103/PhysRevB.78.104118.
[50] J. Bloch, B. Hjörvarsson, S. Olsson, R. Brukas, Reversible structural change and thermodynamic properties of hydrogen in thin vanadium

films, Phys. Rev. B 75 (2007) 165418. https://doi.org/10.1103/PhysRevB.75.165418.
[51] S. Wagner, A. Pundt, Electrical resistivity and hydrogen solubility of PdHc thin films, Acta Materialia 58 (2010) 1387–1394. https://doi.org/10.1016/j.actamat.2009.10.045.
[52] M. Bououdina, J.L. Soubeyroux, P. Juen, C. Mouget, R. Argoud, D. Fruchart, An apparatus for gravimetric analysis: its application to metal-hydrogen systems, Journal of Alloys and Compounds 231 (1995) 422–426. https://doi.org/10.1016/0925-8388(95)01879-4.
[53] K. Komander, T. Tran, J. Saha, M.V. Moro, G.K. Pálsson, M. Wolff, D. Primetzhofer, Interstitial Hydrogen in Fe / V Superstructures: Lattice Site Location and Thermal Vibration, Phys. Rev. Lett. 127 (2021) 136102. https://doi.org/10.1103/PhysRevLett.127.136102.
[54] J.K. Nørskov, Covalent effects in the effective-medium theory of chemical binding: Hydrogen heats of solution in the 3 d metals, Phys. Rev. B 26 (1982) 2875–2885. https://doi.org/10.1103/PhysRevB.26.2875.
[55] R. Griessen, T. Riesterer, Heat of formation models, in: L. Schlapbach (Ed.), Hydrogen in Intermetallic Compounds I, Springer Berlin Heidelberg, Berlin, Heidelberg, 1988: pp. 219–284. https://doi.org/10.1007/3540183337_13.
[56] O.B. Christensen, P.D. Ditlevsen, K.W. Jacobsen, P. Stoltze, O.H. Nielsen, J.K. Nørskov, H-H interactions in Pd, Phys. Rev. B 40 (1989) 1993–1996. https://doi.org/10.1103/PhysRevB.40.1993.
[57] Interstitial Non-stoichiometric Compounds Statistical Thermodynamic Approach to Interstitial Non-stoichiometric Compounds; Hydride, Carbide, Nitride, Phosphide, Sulfide, 1. Aufl, LAP LAMBERT Academic Publishing, Saarbrücken, 2013.
[58] G. Herzberg, A. Monfils, The dissociation energies of the H2, HD, and D2 molecules, Journal of Molecular Spectroscopy 5 (1961) 482–498. https://doi.org/10.1016/0022-2852(61)90111-4.
[59] F.D. Manchester, Lattice gas aspects of metal-hydrogen system, Journal of the Less Common Metals 49 (1976) 1–12. https://doi.org/10.1016/0022-5088(76)90021-7.
[60] W. Pesch, T. Schober, H. Wenzl, A TEM study of the phase diagrams VH and VD, Scripta Metallurgica 16 (1982) 307–312. https://doi.org/10.1016/0036-9748(82)90358-1.
[61] Y. Fukai, S. Kazama, K. Tanaka, M. Matsumoto, Hydrogen-induced states in VHx and VDx observed by soft X-ray emission spectroscopy, Solid State Communications 19 (1976) 507–509. https://doi.org/10.1016/0038-1098(76)90053-3.
[62] P.H. Andersson, L. Fast, L. Nordström, B. Johansson, O. Eriksson, Theoretical study of structural and electronic properties of VH x, Phys. Rev. B 58 (1998) 5230–5235. https://doi.org/10.1103/PhysRevB.58.5230.

[63] C.L. Lai, L.W. Tsay, C. Chen, Effect of microstructure on hydrogen embrittlement of various stainless steels, Materials Science and Engineering: A 584 (2013) 14–20. https://doi.org/10.1016/j.msea.2013.07.004.
[64] T. Schober, A. Carl, A differential thermal analysis study of the vanadium–hydrogen system, Phys. Stat. Sol. (a) 43 (1977) 443–449. https://doi.org/10.1002/pssa.2210430210.
[65] C. Jeynes, R.P. Webb, A. Lohstroh, Ion Beam Analysis: A Century of Exploiting the Electronic and Nuclear Structure of the Atom for Materials Characterisation, in: Reviews of Accelerator Science and Technology, WORLD SCIENTIFIC, 2012: pp. 41–82. https://doi.org/10.1142/9789814383998_0003.
[66] M. Nastasi, J.W. Mayer, Y. Wang, Ion Beam Analysis, 0 ed., CRC Press, 2014. https://doi.org/10.1201/b17310.
[67] R. Holeňák, E. Ntemou, D. Primetzhofer, Charge state distributions of Xenon ions with keV kinetic energies transmitted through graphene and carbon self-supporting foils, Nuclear Instruments and Methods in Physics Research Section B: Beam Interactions with Materials and Atoms 554 (2024) 165415. https://doi.org/10.1016/j.nimb.2024.165415.
[68] G. Schiwietz, P.L. Grande, Improved charge-state formulas, Nuclear Instruments and Methods in Physics Research Section B: Beam Interactions with Materials and Atoms 175–177 (2001) 125–131. https://doi.org/10.1016/S0168-583X(00)00583-8.
[69] J.F. Ziegler, M.D. Ziegler, J.P. Biersack, SRIM – The stopping and range of ions in matter (2010), Nuclear Instruments and Methods in Physics Research Section B: Beam Interactions with Materials and Atoms 268 (2010) 1818–1823. https://doi.org/10.1016/j.nimb.2010.02.091.
[70] J.F. Ziegler, J.P. Biersack, The Stopping and Range of Ions in Matter, in: D.A. Bromley (Ed.), Treatise on Heavy-Ion Science, Springer US, Boston, MA, 1985: pp. 93–129. https://doi.org/10.1007/978-1-4615-8103-1_3.
[71] C.C. Montanari, P. Dimitriou, L. Marian, A.M.P. Mendez, J.P. Peralta, F. Bivort-Haiek, The IAEA electronic stopping power database: Modernization, review, and analysis of the existing experimental data, Nuclear Instruments and Methods in Physics Research Section B: Beam Interactions with Materials and Atoms 551 (2024) 165336. https://doi.org/10.1016/j.nimb.2024.165336.
[72] E. Rutherford, LXXIX. *The scattering of α and β particles by matter and the structure of the atom*, The London, Edinburgh, and Dublin Philosophical Magazine and Journal of Science 21 (1911) 669–688. https://doi.org/10.1080/14786440508637080.
[73] J. L'Ecuyer, J.A. Davies, N. Matsunami, How accurate are absolute rutherford backscattering yields, Nuclear Instruments and Methods 160 (1979) 337–346. https://doi.org/10.1016/0029-554X(79)90612-8.
[74] https://www-nds.iaea.org/exfor/ibandl.htm, (n.d.).

[75] A.F. Gurbich, Evaluation of non-Rutherford proton elastic scattering cross section for oxygen, Nuclear Instruments and Methods in Physics Research Section B: Beam Interactions with Materials and Atoms 129 (1997) 311–316. https://doi.org/10.1016/S0168-583X(97)00288-7.
[76] A.F. Gurbich, SigmaCalc recent development and present status of the evaluated cross-sections for IBA, Nuclear Instruments and Methods in Physics Research Section B: Beam Interactions with Materials and Atoms 371 (2016) 27–32. https://doi.org/10.1016/j.nimb.2015.09.035.
[77] M. Mayer, SIMNRA, a simulation program for the analysis of NRA, RBS and ERDA, in: AIP Conference Proceedings, AIP, Denton, Texas (USA), 1999: pp. 541–544. https://doi.org/10.1063/1.59188.
[78] M.T. Robinson, O.S. Oen, Computer Studies of the Slowing Down of Energetic Atoms in Crystals, Phys. Rev. 132 (1963) 2385–2398. https://doi.org/10.1103/PhysRev.132.2385.
[79] D.S. Gemmell, Channeling and related effects in the motion of charged particles through crystals, Rev. Mod. Phys. 46 (1974) 129–227. https://doi.org/10.1103/RevModPhys.46.129.
[80] K. Komander, M. Moro, J. Saha, M. Wolff, D. Primetzhofer, Hydrogen induced lattice expansion and site occupation analyzed by ion beam methods, Nuclear Instruments and Methods in Physics Research Section B: Beam Interactions with Materials and Atoms 486 (2021) 63–67. https://doi.org/10.1016/j.nimb.2020.09.017.
[81] S.A.E. Johansson, PIXE: a novel technique for elemental analysis, Endeavour 13 (1989) 48–53. https://doi.org/10.1016/0160-9327(89)90002-1.
[82] J.A. Bearden, A.F. Burr, Reevaluation of X-Ray Atomic Energy Levels, Rev. Mod. Phys. 39 (1967) 125–142. https://doi.org/10.1103/RevModPhys.39.125.
[83] J.H. Scofield, Radiative Decay Rates of Vacancies in the K and L Shells, Phys. Rev. 179 (1969) 9–16. https://doi.org/10.1103/PhysRev.179.9.
[84] W.A. Lanford, H.P. Trautvetter, J.F. Ziegler, J. Keller, New precision technique for measuring the concentration versus depth of hydrogen in solids, Applied Physics Letters 28 (1976) 566–568. https://doi.org/10.1063/1.88826.
[85] M. Wilde, K. Fukutani, Hydrogen detection near surfaces and shallow interfaces with resonant nuclear reaction analysis, Surface Science Reports 69 (2014) 196–295. https://doi.org/10.1016/j.surfrep.2014.08.002.
[86] F. Ajzenberg-Selove, Energy levels of light nuclei A = 11−12, Nuclear Physics A 506 (1990) 1–158. https://doi.org/10.1016/0375-9474(90)90271-M.
[87] K. Komander, P. Malinovskis, G.K. Pálsson, M. Wolff, D. Primetzhofer, Accurate measurement of hydrogen concentration in transition metal hydrides utilizing electronic excitations by MeV ions, International Journal of Hydrogen Energy 57 (2024) 583–588. https://doi.org/10.1016/j.ijhydene.2024.01.032.

[88] K. Fukutani, A. Itoh, M. Wilde, M. Matsumoto, Zero-Point Vibration of Hydrogen Adsorbed on Si and Pt Surfaces, Phys. Rev. Lett. 88 (2002) 116101. https://doi.org/10.1103/PhysRevLett.88.116101.
[89] P.J. Kelly, R.D. Arnell, Magnetron sputtering: a review of recent developments and applications, Vacuum 56 (2000) 159–172. https://doi.org/10.1016/S0042-207X(99)00189-X.
[90] D. McKeown, New Method for Measuring Sputtering in the Region Near Threshold, Review of Scientific Instruments 32 (1961) 133–136. https://doi.org/10.1063/1.1717296.
[91] P. Haas, F. Tran, P. Blaha, Calculation of the lattice constant of solids with semilocal functionals, Phys. Rev. B 79 (2009) 085104. https://doi.org/10.1103/PhysRevB.79.085104.
[92] V.G. Tsirelson, A.S. Avilov, Yu.A. Abramov, E.L. Belokoneva, R. Kitaneh, D. Feil, X-ray and Electron Diffraction Study of MgO, Acta Crystallogr B Struct Sci 54 (1998) 8–17. https://doi.org/10.1107/S0108768197008963.
[93] S.A. Droulias, The effect of nano-confinement on hydrogen uptake in metallic superlattices, Uppsala University, Uppsala, 2018.
[94] Y. Wang, G.K. Pálsson, H. Raanaei, B. Hjörvarsson, The influence of amorphous Al2O3 coating on hydrogen uptake of materials, Journal of Alloys and Compounds 464 (2008) L13–L16. https://doi.org/10.1016/j.jallcom.2007.10.045.
[95] The reflection of X-rays by crystals, Proc. R. Soc. Lond. A 88 (1913) 428–438. https://doi.org/10.1098/rspa.1913.0040.
[96] A.L. Patterson, The Scherrer Formula for X-Ray Particle Size Determination, Phys. Rev. 56 (1939) 978–982. https://doi.org/10.1103/PhysRev.56.978.
[97] S.A. Droulias, O. Grånäs, O. Hartmann, K. Komander, B. Hjörvarsson, M. Wolff, G.K. Pálsson, Influence of deuterium-induced volume changes on optical transmission in Fe/V (001) and Cr/V (001) superlattices, Phys. Rev. B 105 (2022) 195438. https://doi.org/10.1103/PhysRevB.105.195438.
[98] S.A. Droulias, G.K. Pálsson, H. Palonen, A. Hasan, K. Leifer, V. Kapaklis, B. Hjörvarsson, M. Wolff, Crystal perfection by strain engineering: The case of Fe/V (001), Thin Solid Films 636 (2017) 608–614. https://doi.org/10.1016/j.tsf.2017.07.005.
[99] P. Ström, D. Primetzhofer, Ion beam tools for nondestructive in-situ and in-operando composition analysis and modification of materials at the Tandem Laboratory in Uppsala, J. Inst. 17 (2022) P04011. https://doi.org/10.1088/1748-0221/17/04/P04011.
[100] T. Tsakiris, K. Komander, M. Wolff, R.J.W. Frost, S.A. Droulias, G.K. Pálsson, D. Primetzhofer, Correlation of optical transmittance and hydrogen concentration in Cr/V superlattices, Nuclear Instruments and

Methods in Physics Research Section B: Beam Interactions with Materials and Atoms 553 (2024) 165398. https://doi.org/10.1016/j.nimb.2024.165398.
[101] D. Moldarev, K. Komander, R. Holeňák, M. Wolff, D. Primetzhofer, A new setup for optical measurements under controlled environment, Review of Scientific Instruments 94 (2023) 035104. https://doi.org/10.1063/5.0142068.
[102] J.S. Larochelle, A. Désilets-Benoit, G. Borduas, S. Laliberté-Riverin, S. Roorda, M. Brochu, Hydrogen loss during N-15 nuclear reaction analysis of high strength steel, Nuclear Instruments and Methods in Physics Research Section B: Beam Interactions with Materials and Atoms 409 (2017) 343–346. https://doi.org/10.1016/j.nimb.2017.03.063.
[103] W.A. Lanford, P. Pelicon, B. Zorko, M. Budnar, Use of reference samples for more accurate RBS analyses, Nuclear Instruments and Methods in Physics Research Section B: Beam Interactions with Materials and Atoms 190 (2002) 410–413. https://doi.org/10.1016/S0168-583X(02)00464-0.
[104] M. Wilde, M. Matsumoto, K. Fukutani, T. Aruga, Depth-resolved analysis of subsurface hydrogen absorbed by Pd(1 0 0), Surface Science 482–485 (2001) 346–352. https://doi.org/10.1016/S0039-6028(01)00727-0.
[105] S. Blässer, J. Steiger, A. Weidinger, In-situ hydrogen charging of thin Nb films and depth profiling with the , αγ) nuclear reaction, Nuclear Instruments and Methods in Physics Research Section B: Beam Interactions with Materials and Atoms 85 (1994) 24–27. https://doi.org/10.1016/0168-583X(94)95778-9.
[106] H. Yonemura, Y. Kitaoka, D. Sekiba, H. Matsuzaki, S. Ogura, M. Matsumoto, Y. Iwamura, T. Ito, T. Narusawa, K. Fukutani, Depth profiling of hydrogen under an atmospheric pressure, Nuclear Instruments and Methods in Physics Research Section B: Beam Interactions with Materials and Atoms 269 (2011) 632–635. https://doi.org/10.1016/j.nimb.2011.01.014.